

Shock–turbulence interactions at high turbulence intensities

Chang Hsin Chen¹ and Diego A. Donzis^{1,†}

¹Department of Aerospace Engineering, Texas A&M University, College Station, TX 77843, USA

(Received 1 June 2018; revised 12 March 2019; accepted 24 March 2019)

Shock–turbulence interactions are investigated using well-resolved direct numerical simulations (DNS) and analysis at a range of Reynolds, mean and turbulent Mach numbers (R_λ , M and M_t , respectively). The simulations are shock and turbulence resolving with R_λ up to 65, M_t up to 0.54 and M up to 1.4. The focus is on the effect of strong turbulence on the jumps of mean thermodynamic variables across the shock, the shock structure and the amplification of turbulence as it moves through the shock. Theoretical results under the so-called quasi-equilibrium (QE) assumption provide explicit laws for a number of statistics of interests which are in agreement with the new DNS data presented here as well as all the data available in the literature. While in previous studies turbulence was found to weaken jumps, it is shown here that stronger jumps are also observed depending on the regime of the interaction. Statistics of the dilatation at the shock are also investigated and found to be well represented by QE for weak turbulence but saturate at high turbulence intensities with a Reynolds number dependence also captured by the analysis. Finally, amplification factors are found to present a universal behaviour with two limiting asymptotic regimes governed by $(M - 1)$ and $K = M_t/R_\lambda^{1/2}(M - 1)$, for weak and strong turbulence, respectively. Effect of anisotropy in the incoming flow is also assessed by utilizing two different forcing mechanisms to generate turbulence.

Key words: compressible turbulence, shock waves, turbulence simulation

1. Introduction and background

Shock–turbulence interactions (STI) are observed in a number of contexts including supersonic aerodynamics, turbulent combustion and astrophysical flows making them an important topic in fluid dynamics. The existence of a shock in a turbulent flow can significantly alter both the mean fields and turbulent characteristics. At the same time, turbulence can also change the structure of a shock. This two-way coupling makes well-known laminar theories predicting, for example, properties jumps across the shock inapplicable in the general case (Lele 1992*b*; Lee, Lele & Moin 1993; Larsson & Lele 2009; Velikovich, Huete & Wouchuk 2012; Larsson, Bermejo-Moreno & Lele 2013). The complexities associated with such flows have made investigations very challenging from the theoretical, experimental and numerical standpoints. To

[†] Email address for correspondence: donzis@tamu.edu

make progress, therefore, it seems necessary to devise flow configurations that reduce complexity yet maintain the essential physics and features of interest. Thus, the canonical interaction of isotropic turbulence with a normal shock has received substantial interest and a large body of literature is devoted to the topic (Sagaut & Cambon 2008; Gatski & Bonnet 2009).

Early theories studied the adjustment of one-dimensional shock waves to changing conditions produced by, e.g. non-uniform media and non-uniform channels (Moeckel 1952; Chisnell 1955; Whitham 1958). However, it was the more general theoretical work of Ribner and Moore (Moore 1954; Ribner 1954*a,b*) who analysed the impingement of different small disturbances on a normal shock in an inviscid flow that provided impetus to the field for decades to come. The incoming disturbance was constructed as a linear combination of simple waves, typically following the first-order decomposition of Kovasznay (1953). If the governing equations and jumps conditions across the shock are linearized, one can obtain a closed solution, known as the linear interaction analysis (LIA). Although LIA can predict, under certain conditions, some of the trends associated with amplification of turbulence, evidence from experiments (Andreopoulos, Agui & Briassulis 2000) and simulations (Lee *et al.* 1993; Mahesh *et al.* 1995; Lee, Lele & Moin 1997; Larsson & Lele 2009; Donzis 2012*a*) have shown that other characteristics of the incoming turbulence not taken into account in the theory can strongly modify the outcome of the interaction. Alternatively, since the shock is essentially a very strong longitudinal velocity gradient, rapid distortion theory (RDT) has also been exploited to provide complementary insight (Jacquin, Cambon & Blin 1993; Kitamura *et al.* 2016). However, RDT was found to overestimate turbulence amplification, in part, due to the non-homogeneous compression induced by the shock (Jacquin *et al.* 1993).

Because of the analytical intractability of the problem, direct numerical simulations (DNS) have become an invaluable tool to seek fundamental insight into STI. A number of DNS studies that investigated STI have also presented comparisons with different theories (Jacquin *et al.* 1993; Lee *et al.* 1993, 1997; Mahesh *et al.* 1995; Mahesh, Lele & Moin 1997; Jamme *et al.* 2002; Larsson & Lele 2009; Larsson *et al.* 2013; Ryu & Livescu 2014; Quadros, Sinha & Larsson 2016*a,b*). A general conclusion from those studies is that turbulence is indeed amplified due to the shock compression. With the enhanced turbulence, various quantities were shown to increase across the shock such as Reynolds stresses, enstrophy and thermodynamic fluctuations. Other variables, on the other hand, were observed to decrease across the shock such as the Taylor and Kolmogorov length scales. Some investigations utilized Kovasznay (1953) decomposition to understand the contributions from different modes (Lee *et al.* 1997; Mahesh *et al.* 1997; Jamme *et al.* 2002; Quadros *et al.* 2016*a*). However, such a method is based on a strong linearization of the fluctuations and is therefore not clear how applicable it is in the case of strong turbulence. Experimental investigations, while very challenging, have also been pursued using different facilities and means of turbulence generation (Honkan & Andreopoulos 1992; Barre, Alem & Bonnet 1996; Agui, Briassulis & Andreopoulos 2005; Inokuma *et al.* 2017). Qualitatively, results are consistent with simulations. However, also consistent with simulations, data suggest that the interaction depends on other characteristics not included in classical theoretical approaches of the incoming turbulence (Agui *et al.* 2005). Indeed, careful comparisons (Donzis 2012*a*) between DNS, experiments, and LIA show significant discrepancies which depend not only on the mean Mach number (M) as predicted by LIA, but also – and more importantly – systematically on the turbulent Mach number (M_t) and the Reynolds number (R_t).

To account for these observed dependencies, the collection of amplification factors of streamwise velocity ($G \equiv u_2'/u_1'^2$, where primes indicate root-mean-square (r.m.s.) quantities and 1 and 2 indicate locations upstream and downstream of the shock) in Donzis (2012a) shows, as mentioned above, systematic trends with Reynolds and turbulent Mach numbers. These observations suggest that some of the assumptions behind LIA (linearity, no viscosity effects, shock wave as a discontinuity) are not satisfied for some conditions. It was then proposed an alternative scaling parameter, K , that includes not only the mean Mach number but also the turbulent Mach number and the Reynolds number. This parameter $K \equiv M_t/R_\lambda^{1/2}(M - 1)$, which can be written as the ratio of shock thickness (δ_i) to Kolmogorov length scale (η), was shown to provide good collapse of the available data. While some new numerical studies have appeared since then, the main focus has been on relatively strong shocks. Regimes where, instead, turbulence is relatively strong – and where assumptions behind classical theories may be inapplicable – have thus received relatively less attention, and is a thrust in this work.

Of interest also is the effect of turbulence on the shock, especially when turbulence is relatively intense. At high enough turbulent intensities it has been found that the shock may present ‘holes’ on its surface along which variables do not undergo a steep change consistent with classical one-dimensional inviscid theoretical results. Instead, variables can change smoothly or present multiple peaks. These two qualitatively distinct regimes have been termed wrinkled and broken (Lee *et al.* 1993; Larsson & Lele 2009) and have been traditionally determined from visual observations of flow fields. To quantify the effects of turbulence on the shock, one can consider the r.m.s.-to-mean ratio of dilatation at the shock, Θ . Under the so-called quasi-equilibrium (QE) assumption (described more precisely below), we have derived an expression for Θ which depends solely on the parameter $M_t/\Delta M$ (Donzis 2012b) where $\Delta M = M - 1$ and that collapsed the data available then. Furthermore, we proposed a mechanisms for the creation of holes due to subsonic regions resulting from strong turbulent fluctuations. While the proposed criterion ($M_t/\Delta M \approx 0.6$) indeed identified correctly wrinkled and broken regimes (Donzis 2012b), no data were available to test directly the appearance of subsonic regions. Here we test this result and extend analytical expressions to the case of strong turbulence.

It has also been observed that turbulence fluctuations can affect the mean properties around the shock. The well-known Rankine–Hugoniot (RH) relations provide an exact solution for the change of properties across a one-dimensional normal shock (Thompson 1984). These expressions depend only on M . When turbulence is present, however, one can expect the results to depend also on turbulent characteristics. Lele (1992b) considered shock jumps of density and pressure in the presence of turbulence using an RDT closure and derived closed expressions for these jumps as a function of M and M_t . However, Larsson *et al.* (2013) suggested that while results were in qualitative agreement with DNS data, there were substantial quantitative disagreements and proposed an empirical dependence on M_t/M instead. In addition to its fundamental importance, understanding the effect of turbulence on mean fields has implications for stability of shock waves in practical devices such as scramjets as well as in simulations of STI. In the latter, corrections to obtain a stationary shock are typically found in a trial-and-error manner (Larsson & Lele 2009; Ryu & Livescu 2014). Thus, there is a clear need to further our fundamental understanding of the effect of turbulence on mean fields, an effort that is undertaken here as well.

The rest of the paper is organized as follows. In §2, the details of the numerical methods used including grid convergence and domain size effects are introduced. In

§ 3, the quasi-equilibrium assumption is described and utilized to obtain thermodynamic jumps and r.m.s.-to-mean dilatation at the shock which are compared with DNS data. Amplification factors are discussed in § 4. Finally, conclusions are presented in § 5.

2. Direct numerical simulations

2.1. Governing equations

The simulations presented here are based on the compressible Navier–Stokes equations:

$$\frac{\partial \rho}{\partial t} + \nabla \cdot (\rho \mathbf{u}) = 0, \quad (2.1)$$

$$\frac{\partial}{\partial t}(\rho \mathbf{u}) + \nabla \cdot (\rho \mathbf{u} \mathbf{u}) = -\nabla p + \nabla \cdot \underline{\boldsymbol{\tau}} + \rho \mathbf{f} + \mathbf{S}, \quad (2.2)$$

$$\frac{\partial}{\partial t}(\rho e) + \nabla \cdot (\rho e \mathbf{u}) = -p \nabla \cdot \mathbf{u} + \nabla \cdot (\kappa \nabla T) + \underline{\boldsymbol{\tau}} \cdot \nabla \mathbf{u} + S_e, \quad (2.3)$$

where ρ is density, \mathbf{u} is the velocity vector, p is pressure, $\underline{\boldsymbol{\tau}}$ is the stress tensor for a Newtonian fluid given by $\tau_{ij} = \mu(\partial u_i / \partial x_j + \partial u_j / \partial x_i - (2/3)\delta_{ij}\partial u_k / \partial x_k)$ with zero bulk viscosity, \mathbf{f} is the body force vector used to generate turbulence, \mathbf{S} is a sponge vector, e is internal energy, κ is thermal conductivity and T is temperature. The viscosity follows a power law with temperature as $\mu = \mu_0(T/T_0)^{0.75}$ (μ_0 and T_0 are reference values) and the Prandtl number is assumed to be constant at $Pr = 0.72$. To close the system of equations, an ideal gas is assumed which follows the equation of state $p = \rho RT$ with R being the gas constant of the fluid. The ratio of specific heats is $\gamma = 1.4$. As in virtually all previous studies (§ 1), the flow is assumed to be a continuum which is justified at the conditions presented here (Moser 2006). As in Donzis & Jagannathan (2013) and Jagannathan & Donzis (2016), discretization of spatial derivatives is performed with tenth-order compact schemes whose numerical and computational advantages are well known (Lele 1992a).

2.2. Numerical methods

In order to assess the generality of the theoretical results presented here, two approaches are used to generate turbulence which yield isotropic and anisotropic fluctuations. The two methods used the same code and adopt the same forcing. The difference between the two approaches lies on where the forcing is applied (S_0) as is seen in the schematic diagrams given in figure 1. This forcing consists of an additional body force in the momentum equation which is stochastic and applied at large scales. This force is constructed using integrated Ornstein–Uhlenbeck processes with finite-time correlation in Fourier space. In physical space, the forcing can be written as

$$\mathbf{f} = \sum_{|\mathbf{k}| < k_F} \hat{\mathbf{f}}_{\perp}(\mathbf{k}) e^{-i\mathbf{k} \cdot \mathbf{x}}, \quad (2.4)$$

where $\hat{\mathbf{f}}_{\perp}(\mathbf{k}) = (\mathbf{I} - \mathbf{k}\mathbf{k}/k^2) \cdot \hat{\mathbf{f}}$ is the projection of the mode at wavenumber \mathbf{k} onto a plane perpendicular to the wave vector itself. This guarantees that the stirring mechanism is, by construction, solenoidal. The forcing parameters are chosen to achieve a given R_{λ} and M_t and, at the same time, yield integral length scales which are a fraction of the domain size. Further details of the forcing and statistics of

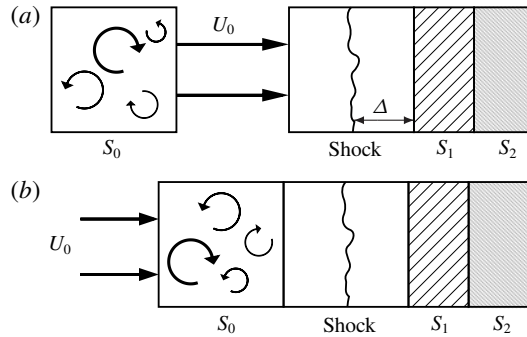


FIGURE 1. A schematic of the shock interacting with (a) isotropic turbulence and (b) anisotropic turbulence in the computational domains.

the resulting turbulence fields are described in Donzis & Jagannathan (2013) and Jagannathan & Donzis (2016).

The two approaches that result in isotropic and anisotropic turbulence, respectively, are now described.

Isotropic turbulence (IT). In this procedure a separate simulation of isotropic turbulence in a triply periodic domain (S_0) is conducted (figure 1a). Once in stationary state, the turbulence is convected through the inlet using Taylor hypothesis at a velocity U_0 which corresponds to a mean Mach number, M . A similar procedure has been used before in the literature with forced (e.g. Ryu & Livescu 2014) and decaying turbulence (e.g. Mahesh *et al.* 1997; Larsson & Lele 2009) though forcing details are somewhat different.

Spatially developing turbulence (SDT). In this approach, turbulence is generated upstream of the shock in S_0 in a single simulation as it is convected at U_0 (figure 1b). The domain is longer in the streamwise direction than that for the isotropic approach above. The interaction between the fluctuations and the mean flow in S_0 , results in unequal production rates in the streamwise and transverse components (Taylor 1935). The result is a slightly anisotropic flow with a streamwise component of the velocity variance larger than transverse components. Such flow is closer to grid-generated turbulence in wind tunnels where anisotropy in the turbulence has been consistently observed (Grant & Nisbet 1957; Mohamed & Larue 1990).

To sustain a statistically stationary shock at a prescribed location in the domain it is necessary to impose a relatively high pressure downstream of the shock which is done here using a sponge region (S_1 in figure 1). For a shock in a uniform flow, the appropriate pressure jump is given by standard Rankine–Hugoniot relations. However, the interaction of turbulent fluctuations with the normal shock produces a well-known slow drift of the shock (Lee *et al.* 1993; Larsson *et al.* 2013; Ryu & Livescu 2014) which is due to the changes in post-shock pressure when upstream fluctuations are present. In a typical STI simulation the back pressure is commonly adjusted in a trial-and-error fashion. Our analytical results below, instead, provide the explicit dependence of pressure jumps on characteristics of the upstream turbulence.

In addition, care has to be taken to avoid boundary reflections as the flow becomes subsonic downstream of the normal shock. Thus, we use a second sponge (S_2 in figure 1) between S_1 and the outlet. In this region the flow is smoothly accelerated to supersonic speeds such that no characteristic travels upstream from the outlet avoiding

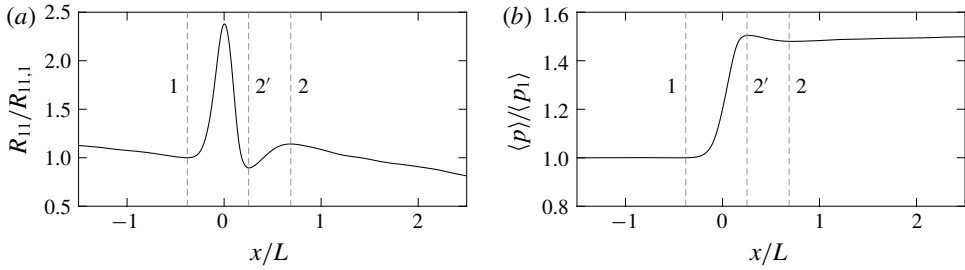


FIGURE 2. Typical streamwise distribution of (a) Reynolds stress R_{11} and (b) pressure, both normalized by their upstream value at $M = 1.2$, $R_\lambda \approx 25$ and $M_t = 0.21$. Vertical dashed lines at x_1 , x_2' and x_2 for reference.

potential effects from outflow boundary conditions. This approach has been used and tested in previous studies (Freund 1997; Ryu & Livescu 2014). In both sponge regions S_1 and S_2 we include a body force of the following form:

$$S_q = A \langle q \rangle \frac{(x - x_{s1})^{n_1} (x - x_{s2})^{n_2}}{l_s^{n_1+n_2+1}} (q_{ref} - q), \quad (2.5)$$

where A is a constant, $\langle \cdot \rangle$ represents an average over the sponge region, x_{s1} and x_{s2} are the beginning and the end points of a sponge, l_s is the length of a sponge, n_1 and n_2 are constant exponents and subscript ‘ref’ stands for the specified value that a variable inside the sponge converges to (pressure in S_1 and streamwise velocity in S_2).

There is some freedom in choosing the sponge parameters, A , n_1 and n_2 . However, we found that some combinations were potentially unstable. From numerical experimentation we found that $(n_1, n_2) = (1, 1)$ in S_1 and $(2, 0)$ in S_2 provide adequate results such that the simulations are stable and both turbulence and shock statistics are insensitive to the parameters in the sponge region.

2.3. Averages and characteristic locations

It is often convenient to decompose the flow using Reynolds decomposition, that is $f = \langle f \rangle + f'$ where $\langle f \rangle$ is a suitably defined mean and f' is the fluctuating part which satisfies $\langle f' \rangle = 0$. In compressible flows, it is also common to use Favre averages (e.g. Gatski & Bonnet 2009) defined as $\tilde{f} = \langle \rho f \rangle / \langle \rho \rangle$. The fluctuations around the Favre averages are denoted by f'' such that $f = \tilde{f} + f''$ and $\langle \rho f'' \rangle = 0$.

The specific space over which averaging is done depends naturally on the flow of interest. In the present simulations, since the streamwise direction (x) is not homogeneous, averages can be taken over the other two homogeneous directions, that is over y - z planes. Furthermore, since the flows presented here are also statistically stationary, one can improve statistical convergence by averaging over time as well. Unless otherwise noted, angular brackets represent plane and time averages in what follows.

We make a few remarks here to identify specific characteristic locations in the flow. Figure 2(a) shows a typical well-resolved (as shown in § 2.4) distribution of the streamwise Reynolds stress, $R_{11} = \overline{u''u''}$, as a function of the streamwise direction. Turbulence enters the domain from the left, and it undergoes a viscous decay. As turbulence reaches the vicinity of the shock, these Reynolds stresses, as well as other

thermodynamic properties such as p (figure 2*b*), begin to increase. The local minimum thus formed has been defined in the literature as the upstream location of the shock and will be denoted here by a subscript 1. Assessing amplification or reduction across the shock can be then performed by normalizing a quantity of interest by its value at this upstream condition. The non-dimensional parameters that characterize the flow are naturally defined at x_1 . These are the mean Mach number of the incoming flow ($M \equiv \langle u_1 \rangle / \langle c \rangle$) which for a stationary shock is also the so-called shock Mach number, the Taylor Reynolds number ($R_\lambda \equiv \langle \rho \rangle u_{1,rms} \lambda / \langle \mu \rangle$) and the turbulent Mach number ($M_t \equiv \widetilde{|\mathbf{u}''\mathbf{u}''|}^{1/2} / \langle c \rangle$).

Inside the shock region, stresses reach a peak at a location where the pressure gradient is largest. Reynolds stresses then decrease and reach a downstream minimum where pressure attains a maximum. This location, identified as $2'$, indicates the end of the region dominated by shock compression. An expansion wave would follow behind the shock (Larsson & Lele 2009) where the stress reaches its downstream maximum. This process is dominated by pressure-dilatation exchanges that transfer internal energy to turbulent kinetic energy (Lee *et al.* 1993). The Reynolds stresses increase but eventually viscous dissipation dominates the energy exchanges and turbulence undergoes again a classical viscous decay. The local maximum of R_{11} downstream of the shock is denoted here by a subscript 2.

2.4. Resolution and DNS database

In table 1 we summarize the parameters for the simulations of STI with IT. The incoming turbulence is at turbulent Mach numbers ranging from 0.05 to 0.54 and Reynolds numbers up to 65. These parameters are obtained at location x_1 . The table also includes the ratio of Kolmogorov length scale to grid size $\eta/\Delta x$, and the shock thickness to grid size, $\delta_i/\Delta x$, where (Thompson 1984) $\delta_i = 2k_1\langle\mu_1\rangle/(\langle c_1\rangle\langle\rho_1\rangle\Delta M)$ with $k_1 = (4/3 + (\gamma - 1)/Pr)$. In our simulations $k_1 \sim O(1)$. We have also included the classification of the regime of the interaction based on the mechanism in Donzis (2012*b*) where a transition from wrinkled to broken was proposed at $M_t/\Delta M \approx 0.6$, consistent with the regimes observed in the literature (Larsson *et al.* 2013; Ryu & Livescu 2014).

To ensure grid independence, convergence tests were conducted to assess the sensitivity of variables that characterize both large and, more critically, small scales. Two quantities that satisfy these requirements are the streamwise Reynolds stress, specifically its amplification factor, and the maximum dilatation at the shock. The latter is critically sensitive to resolution as it is computed at a location where gradients are largest (inside the viscous shock). In fact, this is a very strict resolution criterion but necessary for well-resolved shock-resolving simulations. In figure 3, we show the typical behaviour of the amplification factor of streamwise velocity, $G = R_{11,2}/R_{11,1}$ and r.m.s.-to-mean dilatation Θ (Donzis 2012*b*) as the ratio of shock thickness to grid spacing is increased. We see that beyond $\delta_i/\Delta x \approx 4.5$, changes in these quantities are within 2% and are thus considered grid converged. Similar results have been observed for the other conditions in our database. In addition, we have found (Jagannathan & Donzis 2016) that a resolution of $\eta/\Delta x \approx 0.5$ is sufficient in isotropic turbulence to capture even fourth-order moments of velocity gradients at the conditions presented here. From tables 1 and 2 we can see that resolving the shock wave provides a stricter resolution criterion. In the table we also include $\langle\delta_i\rangle$, the average thickness of the shock when turbulence is present (Donzis 2012*b*) which is here computed as $(\langle u_2 \rangle - \langle u_1 \rangle) / (\partial\langle u \rangle/\partial x)_{max}$. As expected and consistent with theoretical predictions

| Grid | M | R_λ | M_t | $\delta_l/\Delta x$ | $\langle\delta_t\rangle/\Delta x$ | $\eta/\Delta x$ | Regime |
|---------------------|-----|-------------|-------|---------------------|-----------------------------------|-----------------|-----------|
| 1024×256^2 | 1.1 | 12 | 0.05 | 4.89 | 11.0 | 8.58 | Wrinkled |
| 512×128^2 | 1.1 | 10 | 0.08 | 4.84 | 9.4 | 4.86 | Broken |
| 512×128^2 | 1.1 | 10 | 0.14 | 8.42 | 17.1 | 4.96 | Broken |
| 256×128^2 | 1.1 | 11 | 0.22 | 6.90 | 13.9 | 2.55 | Broken |
| 256×128^2 | 1.1 | 11 | 0.29 | 10.14 | 16.3 | 2.65 | Broken |
| 256×128^2 | 1.1 | 11 | 0.34 | 13.31 | 17.2 | 2.82 | Vanished* |
| 1024×256^2 | 1.1 | 27 | 0.13 | 4.85 | 23.8 | 4.65 | Broken |
| 512×128^2 | 1.1 | 24 | 0.22 | 4.57 | 25.8 | 2.56 | Broken |
| 512×128^2 | 1.1 | 25 | 0.30 | 6.99 | 29.5 | 2.68 | Broken |
| 512×256^2 | 1.1 | 24 | 0.44 | 12.83 | 50.0 | 3.05 | Vanished* |
| 2048×512^2 | 1.2 | 12 | 0.05 | 4.86 | 15.6 | 17.7 | Wrinkled |
| 1024×256^2 | 1.2 | 11 | 0.08 | 4.85 | 14.5 | 9.80 | Wrinkled |
| 512×128^2 | 1.2 | 10 | 0.14 | 4.53 | 12.3 | 4.94 | Broken |
| 512×128^2 | 1.2 | 12 | 0.22 | 7.42 | 19.6 | 5.05 | Broken |
| 256×128^2 | 1.2 | 13 | 0.39 | 5.82 | 16.6 | 2.48 | Broken |
| 2048×512^2 | 1.2 | 27 | 0.12 | 4.85 | 34.4 | 9.42 | Broken |
| 1024×256^2 | 1.2 | 24 | 0.21 | 4.82 | 36.4 | 5.14 | Broken |
| 1024×256^2 | 1.2 | 23 | 0.32 | 7.24 | 43.2 | 5.23 | Broken |
| 512×256^2 | 1.2 | 25 | 0.44 | 5.34 | 49.9 | 2.82 | Broken |
| 2048×512^2 | 1.2 | 47 | 0.34 | 4.69 | 84.5 | 4.61 | Broken |
| 1536×512^2 | 1.2 | 42 | 0.42 | 5.36 | 84.9 | 4.10 | Broken |
| 4096×512^2 | 1.2 | 62 | 0.28 | 4.86 | 129 | 6.48 | Broken |
| 2048×512^2 | 1.2 | 65 | 0.51 | 5.05 | 109 | 3.64 | Broken |
| 2048×512^2 | 1.4 | 23 | 0.23 | 4.82 | 45.6 | 9.51 | Wrinkled |
| 1536×512^2 | 1.4 | 25 | 0.33 | 5.45 | 48.8 | 7.78 | Broken |
| 1024×256^2 | 1.4 | 23 | 0.45 | 5.58 | 61.2 | 5.47 | Broken |
| 1024×256^2 | 1.4 | 24 | 0.54 | 6.32 | 61.8 | 5.35 | Broken |

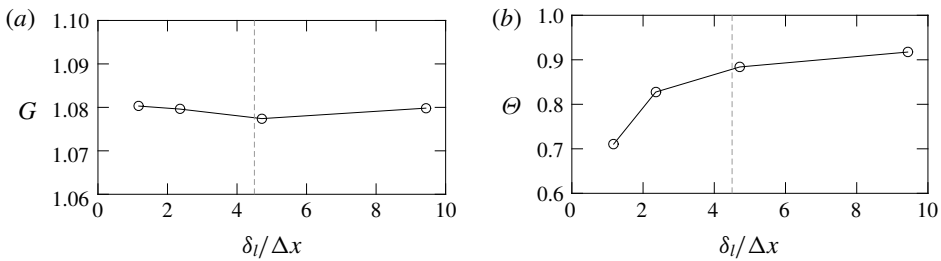
TABLE 1. DNS database of isotropic turbulence (IT) passing through a shock: number of grid points, mean Mach number (M), turbulent Mach (M_t), Taylor Reynolds numbers (R_λ), normalized shock thicknesses and Kolmogorov length scale. The wrinkled and broken regimes correspond to the criterion in Donzis (2012*b*). Conditions for vanished regimes (marked with *) are computed at the upstream minimum for pressure (§ 3.3).

(Donzis 2012*b*), the difference between δ_l and $\langle\delta_t\rangle$ increases with M_t . We do note that these definitions are estimates based on the maximum gradient at the shock and upon inspection represent only a fraction of the actual spatial extent occupied by the shock. In fact, even for the most stringent condition, at least 20 grid points are located between x_1 and x_2 (see figure 2). As mentioned above, however, this is for the most stringent cases and, as seen in the tables, most simulations have a larger number of grid points in the shock region. We have also verified grid convergence in the transverse direction since downstream of the shock, the Kolmogorov scale is reduced (Larsson & Lele 2009). At the most stringent conditions, we see a reduction of $\sim 30\%$ in η which when evaluated with our resolutions (tables 1 and 2) results in $\eta/\Delta y \approx 1.8$ which is also grid converged (Jagannathan & Donzis 2016) for all cases here.

To ensure the sponges downstream of the shock have negligible effect on the interaction, we have conducted simulations with varying distance between the shock and the sponges, Δ (see figure 1). The results are seen in figure 4 where we show

| Grid | M | R_λ | M_t | R_{11}/R_{22} | $\delta_l/\Delta x$ | $\langle \delta_l \rangle / \Delta x$ | $\eta/\Delta x$ | Regime |
|---------------------|------|-------------|-------|-----------------|---------------------|---------------------------------------|-----------------|-----------|
| 384×128^2 | 1.07 | 5 | 0.15 | 1.24 | 25.9 | 25.11 | 5.86 | Vanished* |
| 768×128^2 | 1.1 | 4 | 0.02 | 1.26 | 8.55 | 9.15 | 13.6 | Wrinkled |
| 384×128^2 | 1.1 | 5 | 0.04 | 1.25 | 6.98 | 7.65 | 6.33 | Wrinkled |
| 384×128^2 | 1.1 | 5 | 0.07 | 1.33 | 11.7 | 12.2 | 6.47 | Broken |
| 384×128^2 | 1.1 | 5 | 0.12 | 1.57 | 15.8 | 17.1 | 6.14 | Broken |
| 768×128^2 | 1.1 | 13 | 0.06 | 1.11 | 4.88 | 9.96 | 5.23 | Wrinkled |
| 512×128^2 | 1.1 | 12 | 0.09 | 1.29 | 5.77 | 10.4 | 4.36 | Broken |
| 384×128^2 | 1.1 | 13 | 0.13 | 1.47 | 5.94 | 10.6 | 3.27 | Broken |
| 384×128^2 | 1.1 | 10 | 0.16 | 1.10 | 7.30 | 13.7 | 3.25 | Broken |
| 768×128^2 | 1.2 | 7 | 0.07 | 1.40 | 6.95 | 10.04 | 9.92 | Wrinkled |
| 384×128^2 | 1.2 | 5 | 0.09 | 1.37 | 7.37 | 9.25 | 6.49 | Wrinkled |
| 384×128^2 | 1.2 | 5 | 0.12 | 1.48 | 8.20 | 10.9 | 6.06 | Broken |
| 384×128^2 | 1.2 | 5 | 0.16 | 1.64 | 9.37 | 13.2 | 5.75 | Broken |
| 1536×256^2 | 1.2 | 13 | 0.05 | 1.44 | 4.75 | 11.0 | 12.9 | Wrinkled |
| 896×128^2 | 1.2 | 12 | 0.08 | 1.23 | 4.86 | 10.6 | 8.34 | Wrinkled |
| 512×128^2 | 1.2 | 13 | 0.16 | 1.48 | 4.98 | 12.6 | 4.38 | Broken |

TABLE 2. DNS database of anisotropic turbulence (SDT).

FIGURE 3. Grid-independence test with different $\delta_l/\Delta x$ at $M = 1.1$, $M_t = 0.21$ and $R_\lambda \approx 25$ for (a) amplification factor and (b) r.m.s.-to-mean dilatation. The dashed line represents $\delta_l/\Delta x = 4.5$.

the distribution of R_{11} different values of Δ . While all cases appear to collapse, some shock drifting is actually observed at $\Delta = 0.5\pi$. This is more evident in figure 5 where we present G and Θ for different values of Δ . Differences in this quantities for $\Delta \gtrsim \pi$ are negligibly small. While data with $\Delta = 0.5\pi$ are also close, as a conservative measure especially at high M_t , we have used $\Delta = \pi$. For reference, we mention that this distance corresponds to $\Delta \approx 2L$ where L is the integral scale of the incoming turbulence.

3. Turbulent shock jumps and shock structure

3.1. Theoretical background: quasi-equilibrium assumption and truncated integrals

Available results in the literature clearly show that characteristics of STI depend critically on the strength of turbulence (Andreopoulos *et al.* 2000) which is not captured by LIA. The theoretical work of Moeckel (1952), Chisnell (1955), Whitham (1958), is also unable to capture the complex behaviour of STI because of its simplified configuration and restrictive assumptions. An alternative view was more

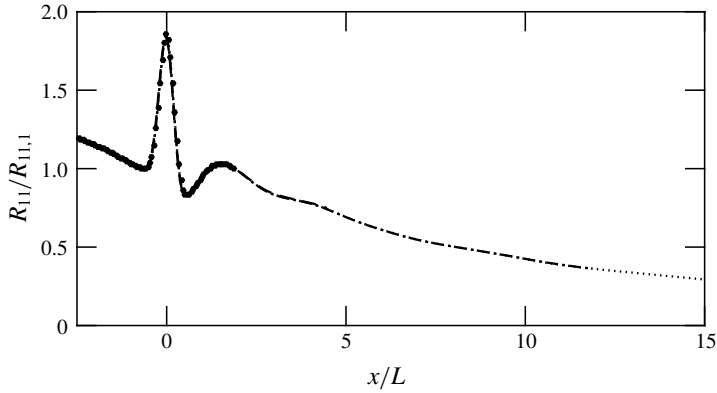


FIGURE 4. Distribution of R_{11} at $M = 1.2$, $M_t = 0.23$ and $R_\lambda \approx 10$ with $\Delta = 0.5\pi$ (\bullet), 1.1π (dashed), 2.2π (dash-dotted) and 3.3π (dotted).

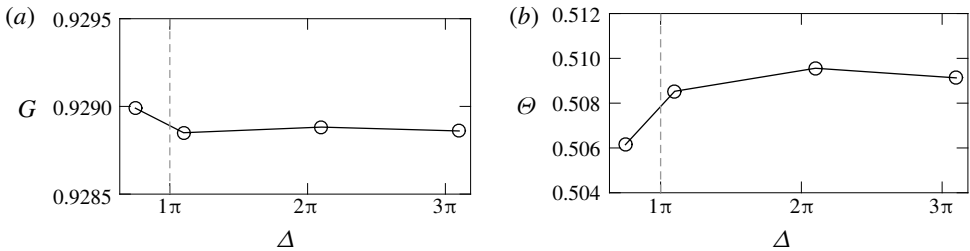


FIGURE 5. Test of distance between shock and sponges for (a) G and (b) Θ at $M = 1.2$, $M_t = 0.23$ and $R_\lambda \approx 10$.

recently put forward (Donzis 2012b), in which it was assumed that the shock, locally, adjusts instantaneously to local flow conditions. This was referred to as the quasi-equilibrium assumption. If conditions are such that QE is satisfied, a shock in a turbulent flow can be treated as consisting of a collection of infinitesimal shocks each obeying RH relations based on local flow conditions. For QE to be valid, the time scale associated with the relaxation of the shock to a new incoming condition should be much shorter than changes in upstream conditions produced by the turbulence. We showed (Donzis 2012b) that this is justified when $K \ll 1$ which is satisfied for virtually all cases in the literature. The main advantage of QE is that it provides a framework in which well-known laminar results can be used to analytically compute mean variables in STI. In this section we use QE to provide analytical results for thermodynamic jumps across the shock. For strong turbulence, however, we first need to introduce a generalization of the analysis (Donzis 2012b) which requires a redefinition of integrals to compute statistical moments across planes parallel to the shock surface.

Consider a shock in a uniform flow and a quantity q that depends on the upstream Mach number, M , that is $q = q(M)$. In the presence of turbulent fluctuations, QE allows one to still write q as a function of the local instantaneous Mach number, that is $q = q(M + m)$ where m is the fluctuating Mach number. In general, the n th-order

moment of q is given by the integral

$$\langle q^n \rangle = \int_{-\infty}^{\infty} q^n (M + m) f_m(m) dm, \quad (3.1)$$

where $f_m(m)$ is the probability density function (p.d.f.) of m . Note that $M + m$ is to be taken as the relative velocity between the shock and the upstream flow. Thus, while here we consider a stationary shock, this formulation can account for moving shocks by a simple Galilean transformation.

However, the actual functional form of $q(M + m)$ may depend on whether the flow is supersonic or subsonic. For example, in locations where the flow is supersonic upstream of the mean location of the shock, the pressure will change according to the RH relations. However, if the flow is subsonic (due to strong negative m fluctuations), then RH relations are invalid. This, as argued in Donzis (2012b), creates holes in the shock surface.

For the flow to be supersonic one needs $M + m > 1$ or, in terms of $\Delta M = M - 1$, one needs $m > -\Delta M$. Similarly subsonic regions correspond to fluctuations that satisfy $m < -\Delta M$. Thus, we split the integral in (3.1) as

$$\langle q^n \rangle = \int_{-\Delta M}^{\infty} (q^>)^n f_m(m) dm + \int_{-\infty}^{-\Delta M} (q^<)^n f_m(m) dm, \quad (3.2)$$

where $q^>$ and $q^<$ are the functional form of q in supersonic and subsonic regions, respectively. For short, the supersonic and subsonic integrals will be denoted by $\langle q^n \rangle^>$ and $\langle q^n \rangle^<$, respectively, that is

$$\langle q^n \rangle = \langle q^n \rangle^> + \langle q^n \rangle^<. \quad (3.3)$$

One can, for example, compute moments of the fluctuating Mach number itself, i.e. $q = m$, for which supersonic and subsonic expressions are the same ($q^> = q^<$). In this case we have:

$$\langle m^n \rangle^> = \int_{-\Delta M}^{\infty} m^n f_m(m) dm, \quad \langle m^n \rangle^< = \int_{-\infty}^{-\Delta M} m^n f_m(m) dm. \quad (3.4a,b)$$

Obviously, $\langle m^0 \rangle = 1$ and $\langle m \rangle = 0$. Also note that by definition we can write the turbulent Mach number as:

$$M_t = \sqrt{3} \langle m^2 \rangle^{1/2} = \sqrt{3} \left(\int_{-\infty}^{\infty} m^2 f_m(m) dm \right)^{1/2} \quad (3.5)$$

regardless of the specific velocity distribution.

It is well known that the velocity field in isotropic turbulence is generally well represented by a Gaussian distribution (Batchelor 1953; Monin & Yaglom 1975). This is indeed the case for our data as seen in figure 6 where we show even moments of the streamwise velocity component and Mach number from our DNS database. Gaussian values are included as horizontal dashed lines for reference. We also see a slight sub-Gaussian behaviour for very high orders which has also been observed before (Noullez *et al.* 1997; Jimenez 1998). In any case, our results will rely on at most second-order statistics for which a Gaussian behaviour is an excellent

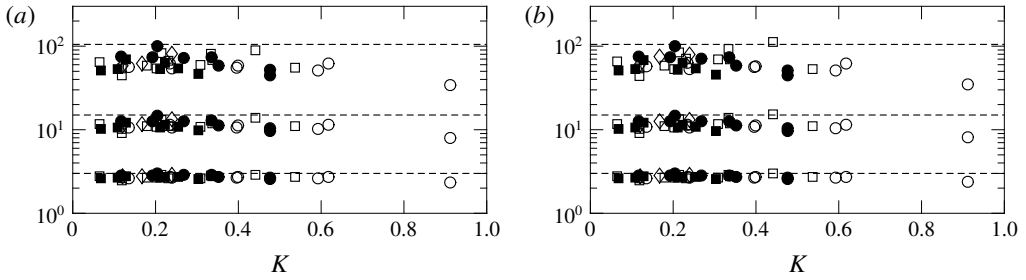


FIGURE 6. Even moments of (a) velocity fluctuation $\langle u^n \rangle / \langle u^2 \rangle^{n/2}$ and (b) Mach number fluctuation $\langle m^n \rangle / \langle m^2 \rangle^{n/2}$ as functions of K at location 1 for all the simulations in tables 1 and 2: $M = 1.1$ (circles), $M = 1.2$ (squares) and $M = 1.4$ (diamonds). Open and closed symbols are for IT and SDT simulations. From bottom to top $n = 4, 6$ and 8 . Dashed lines correspond to Gaussian values at 3, 15 and 105, respectively.

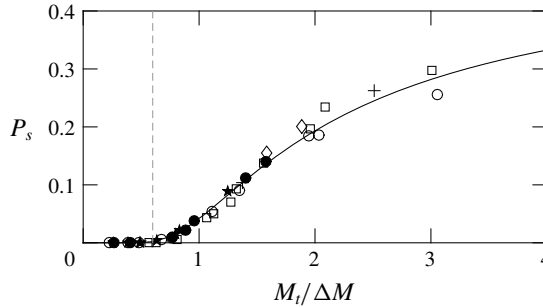


FIGURE 7. Probability of subsonic regions upstream of the shock. Solid line: theoretical $P_s = P(m < -\Delta M)$ with Gaussian p.d.f. for m . Symbols for DNS data at $R_\lambda \approx 5$ (stars), $R_\lambda \approx 10$ (circles), $R_\lambda \approx 25$ (squares), $R_\lambda \approx 45$ (diamonds) and $R_\lambda \approx 65$ (plus signs). Open and closed symbols are for IT and SDT simulations, respectively. Grey dashed line at $M_t / \Delta M = 0.6$ for reference.

approximation. For reference, the first few truncated moments of m for a Gaussian distribution are shown in appendix A.

In Donzis (2012b) we argued that, consistent with QE, holes in the shocks are caused by locally subsonic conditions. Then $\langle m^0 \rangle^<$ would represent the fraction of the shock with subsonic regions and, thus, holes. This analytical form is shown in figure 7. One can see that the subsonic fraction upstream of the shock is negligible for $M_t / \Delta M \lesssim 0.6$ but grows quickly with $M_t / \Delta M$ beyond that. Thus, one expects to observe holes only at $M_t / \Delta M \gtrsim 0.6$ (Donzis 2012b) in what is now called the broken regime. This criterion has indeed been supported by more recent DNS data (Larsson *et al.* 2013). In the figure we also include results from our own DNS taken as the fraction of subsonic regions observed at x_1 . The excellent agreement supports both the Gaussian assumption for m as well as the criterion $M_t / \Delta M = 0.6$ to delineate the boundary between wrinkled and broken regimes. The last column in tables 1 and 2 indicates the regime based on this criterion.

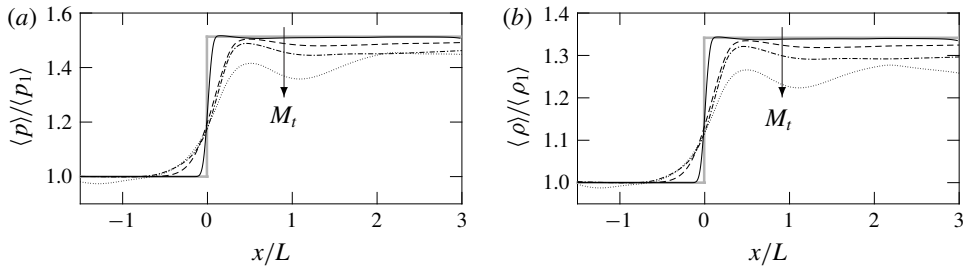


FIGURE 8. (a) Pressure and (b) density profile of normal shocks interacting with isotropic turbulence at $M = 1.2$, $R_\lambda \approx 25$ and $M_t = 0.12$ (solid), 0.21 (dashed), 0.32 (dashed-dotted) and 0.44 (dotted). Grey lines correspond to the laminar inviscid limit, namely, RH jumps.

3.2. Analytical solutions of turbulent shock jumps

3.2.1. Density, pressure and temperature

The Rankine–Hugoniot relations, which relate upstream and downstream conditions of a shock in a uniform flow, are a function of M alone. In turbulent flows, however, fluctuations are found to modify these jumps, an effect that is more prominent as the strength of turbulence increases. This can be seen in figure 8 where we plot the distributions of pressure and density for different values of M_t . As M_t increases the jumps weaken compared to RH jumps (horizontal dotted lines) at a fixed M . These results demonstrate that thermodynamic jumps depend not only on the mean flow but also on turbulent fluctuations. This effect is not captured by classical theories such as LIA whose results depend only on M . Our objective here is to obtain analytical solutions for jumps of thermodynamic variables that can account for the effects of turbulence.

Consider first the ratio of mean density upstream and downstream of the shock, that is, $\langle \rho_2 \rangle / \langle \rho_1 \rangle$. To compute this ratio we will obtain $\langle \rho_1 \rangle$ and $\langle \rho_2 \rangle$ in turn. We first note that in general the mean density ahead of a shock depends on the levels of fluctuations. A convenient way to account for this is to write the instantaneous density upstream of the shock in terms of stagnation conditions,

$$\rho_1 = \left[\frac{\gamma - 1}{2} (M + m)^2 + 1 \right]^{-1/(\gamma-1)} \rho_{01}, \quad (3.6)$$

where subscript 0 indicates a stagnation property. If fluctuations are isentropic, then ρ_{01} would be a constant across a plane parallel to the shock (over which averages are taken) independent of local Mach number fluctuations. This is in fact a very reasonable approximation for fluctuations not very far from the mean (Donzis & Jagannathan 2013) and will, thus, be adopted here.

Expanding (3.6) in Taylor series around the mean Mach number yields:

$$\rho_1 = \rho_1|_{m=0} + \left(\frac{\partial \rho_1}{\partial m} \right)_{m=0} m + \frac{1}{2} \left(\frac{\partial^2 \rho_1}{\partial m^2} \right)_{m=0} m^2 + \dots, \quad (3.7)$$

whose average can then be computed by

$$\langle \rho_1 \rangle = \int_{-\infty}^{\infty} \rho_1 f_m(m) dm. \quad (3.8)$$

Combining (3.6)–(3.8) and a Gaussian $f_m(m)$ (see table 3) we can obtain the final form for the mean upstream density:

$$\langle \rho_1 \rangle = \mathbb{M}^{-1/(\gamma-1)} \rho_{01} + \frac{1}{12} \mathbb{M}^{(-2\gamma+1)/(\gamma-1)} [(\gamma+1)M^2 - 2] \rho_{01} M_t^2, \tag{3.9}$$

where, for simplicity in notation, we have defined $\mathbb{M} \equiv (\gamma-1)M^2/2 + 1$. The first term in (3.9) corresponds to the laminar contribution while the second term corresponds to turbulence effects which depend explicitly on both M and M_t . Clearly, as $M \rightarrow \infty$ or $M_t \rightarrow 0$, the second term vanishes, as expected.

Under the QE assumption, the density immediately downstream of the shock (i.e. location 2') will be given by RH expressions using the local Mach number, that is

$$\rho_{2'}^> = \frac{(\gamma+1)(M+m)^2}{(\gamma-1)(M+m)^2 + 2} \rho_{01}. \tag{3.10}$$

The superscript $>$ has been added to emphasize that shock relations are valid only for supersonic regions. Using (3.6), the expression becomes:

$$\rho_{2'}^> = \left[\frac{(\gamma+1)(M+m)^2}{(\gamma-1)(M+m)^2 + 2} \right] \left[\frac{\gamma-1}{2} (M+m)^2 - 1 \right]^{-1/(\gamma-1)} \rho_{01}. \tag{3.11}$$

In subsonic regions this expression is clearly invalid and, thus, averages need to be taken using the split form in (3.3). For subsonic regions, where shock holes appear, one can assume that variables will approximately retain their upstream value. That is, $\rho_{2'}^< \approx \rho_1$. This assumption is indeed supported by observations of instantaneous density profiles in the broken regime (e.g. Larsson & Lele 2009). Hence, the average downstream density is given by:

$$\langle \rho_{2'} \rangle = \langle \rho_{2'}^> \rangle + \langle \rho_1 \rangle^<. \tag{3.12}$$

Again, using Taylor series for (3.11) and substituting into (3.12) one can integrate the expressions analytically with $f_m(m)$ Gaussian, to obtain

$$\begin{aligned} \langle \rho_{2'} \rangle &= \left[\frac{(\gamma+1)M^2}{(\gamma-1)M^2 + 2} \right] \mathbb{M}^{-1/(\gamma-1)} \rho_{01} \langle m^0 \rangle^> - \frac{\gamma+1}{2} M(M^2 - 2) \mathbb{M}^{(-2\gamma+1)/(\gamma-1)} \rho_{01} \langle m \rangle^> \\ &+ \frac{\gamma+1}{8} \mathbb{M}^{(-3\gamma+2)/(\gamma-1)} [(\gamma+1)M^4 - (6\gamma+4)M^2 + 4] \rho_{01} \langle m^2 \rangle^> \\ &+ \mathbb{M}^{-1/(\gamma-1)} \rho_{01} \langle m^0 \rangle^< - M \mathbb{M}^{-\gamma/(\gamma-1)} \rho_{01} \langle m \rangle^< \\ &+ \frac{1}{4} \mathbb{M}^{(-2\gamma+1)/(\gamma-1)} [(\gamma+1)M^2 - 2] \rho_{01} \langle m^2 \rangle^<, \end{aligned} \tag{3.13}$$

which, though very complicated, provides an analytical closed form for the mean density downstream of a shock as a function of both M and M_t .

Thus the density jump across a shock in a turbulent flow with mean Mach number M and turbulent Mach number M_t can be written as

$$\frac{\langle \rho_{2'} \rangle}{\langle \rho_1 \rangle} = g_\rho(M, M_t), \tag{3.14}$$

where $g_\rho(M, M_t)$ is the ratio of (3.13) and (3.6).

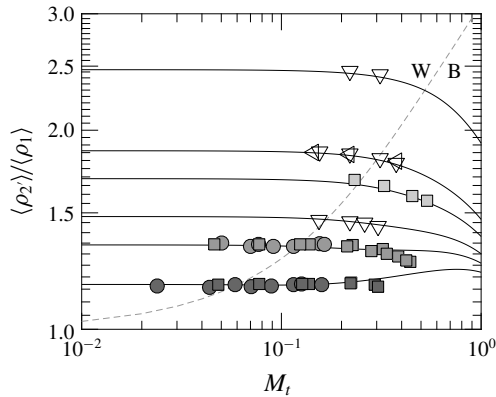


FIGURE 9. Mean density jumps from IT (squares) and SDT (circle) simulations at $M = 1.1$ (dark), 1.2 (medium) and 1.4 (light). Other symbols are for Larsson & Lele (2009) (∇), and Larsson *et al.* (2013) (\triangleleft). Solid lines correspond to the analytical solution (3.14) at $M = 1.1, 1.2, 1.28, 1.4, 1.5$ and 1.87 (bottom to top). Grey dashed line at $M_t/\Delta M = 0.6$ separates the wrinkled (W) and broken (B) regimes.

In figure 9 we show $\langle \rho_2 \rangle / \langle \rho_1 \rangle$ from DNS data as a function of M_t along with (3.14). We see very good agreement between DNS data from various sources (symbols) and the theoretical prediction (solid lines). As expected, laminar conditions are recovered as the turbulent Mach number decreases which is seen as solid lines approach their asymptotic RH value at $M_t \rightarrow 0$. It is interesting to note that the effect of turbulent fluctuations depends on the mean Mach number as well. In particular, stronger turbulence effects are observed at higher M . This suggests an interaction between means and fluctuations which is not accounted for in classical theories such as LIA. For relatively high M , an increase in turbulence intensity measured by M_t , results in weakened jumps relative to the laminar situation consistent with previous observations (Larsson *et al.* 2013). It is worth mentioning here, that mean jumps are unaffected by turbulence within LIA and can thus not capture this behaviour. Predictions using RDT, in turn, were also found (Larsson *et al.* 2013) to remain only qualitatively consistent with the data. The quantitative agreement between (3.14) and data observed in figure 9, thus, provides support to the adequacy of the QE coupled with the isentropic assumption of upstream fluctuations to capture this two-way coupling.

We also see a qualitative change in the effect of turbulence as M decreases. For relatively weak shocks (low M) the theory predicts stronger shock jumps as turbulence intensity increases. Our DNS data do indeed show a consistent, though small, increase with M_t . This low- M conditions may be important in situations around transients crossing sonic conditions such as bodies, vanes or blades accelerating to supersonic speeds or decelerating to subsonic speeds. At $M \approx 1.2$, jumps appear to be only weakly affected by turbulence with jumps remaining fairly constant with M_t . This transition M , however, is not general and depends on the value of γ .

In figure 9 we also show a (dashed) line at constant $M_t/\Delta M = 0.6$ which separates the wrinkled (denoted W in the figure) and broken (denoted B) regimes (Donzis 2012*b*). Conditions to the left of the WB line correspond to wrinkled interactions where the planar shock retains its structure and is only mildly distorted by the relatively weak incoming turbulent fluctuations. To the right of that line, the

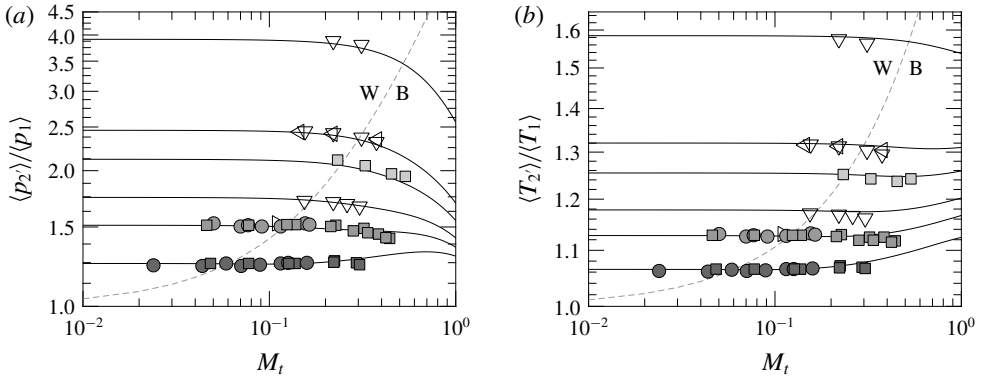


FIGURE 10. Mean pressure and temperature jumps from IT (squares) and SDT (circles) simulations, Lee *et al.* (1993) (\triangleright), Larsson & Lele (2009) (∇) and Larsson *et al.* (2013) (\triangleleft). Solid lines correspond to the analytical solution (A 5) at $M = 1.1, 1.2, 1.28, 1.4, 1.5$ and 1.87 (bottom to top). Grey dashed line at $M_t / \Delta M = 0.6$ separates the wrinkled (W) and broken (B) regimes.

interaction is in the broken regime where holes appear across the shock. As M_t is increased further, which implies also high K , the fundamental assumptions behind QE will become progressively less applicable. These include the inability of the shock to adjust instantaneously to changing conditions due to turbulence fluctuations (Donzis 2012b) as well as strong three-dimensional effects. This can explain the discrepancy seen between theory and DNS data for high- M_t low- M interactions in figure 9.

Following the same procedure described above, one can obtain expressions for $\langle p_1 \rangle$, $\langle p_2 \rangle$, $\langle T_1 \rangle$ and $\langle T_2 \rangle$. The final result is

$$\frac{\langle p_2 \rangle}{\langle p_1 \rangle} = g_p(M, M_t), \tag{3.15}$$

$$\frac{\langle T_2 \rangle}{\langle T_1 \rangle} = g_T(M, M_t). \tag{3.16}$$

The details of the derivation and final expressions can be found in appendix A.

The comparison between DNS data and (3.15) and (3.16) is shown in figure 10. Again, good agreement is observed at a range of M_t . While the behaviour of pressure is very similar to that of density we see that that of temperature is not. In fact, trends appear inverted: at low M effects are stronger and jumps become larger as M_t increases. At high M , effects are weaker and there is a slight decrease in jumps as M_t increases.

3.2.2. Comparison to Rankine–Hugoniot relations

While it has been argued in the literature that stronger turbulence leads to weakened shock jumps (Larsson & Lele 2009), the data presented here suggest a more complex interaction. In particular, whether turbulence weakens or strengthens shock jumps depends on the specific combination of M_t and M . The theoretical results here can, in fact, provide the necessary guidance to understand this observation. Consider the

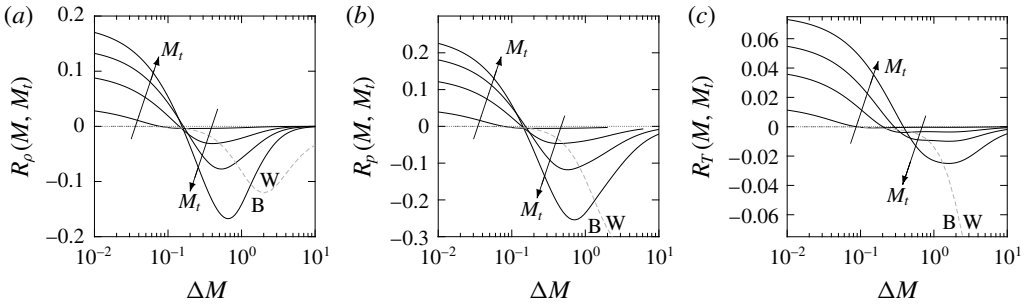


FIGURE 11. Relative departures from RH jumps for (a) density $R_\rho(M, M_t)$, (b) pressure $R_p(M, M_t)$ and (c) temperature $R_T(M, M_t)$ at $M_t = 0.1, 0.3, 0.5$ and 0.8 . Grey dashed line at $M_t/\Delta M = 0.6$ separates the wrinkled (W) and broken (B) regimes.

relative change of the density jump $\langle \rho_2 \rangle / \langle \rho_1 \rangle = g_\rho(M, M_t)$ with respect to the RH jump, $g_\rho^{RH}(M)$:

$$R_\rho(M, M_t) = \frac{g_\rho(M, M_t) - g_\rho^{RH}(M)}{g_\rho^{RH}(M)}. \quad (3.17)$$

This function, which with (3.14) is known analytically, provides direct information of the effect of turbulence on the jumps of mean thermodynamic quantities. This is shown in figure 11(a) where we can now clearly see that turbulence effects on jumps depend on both M and M_t . In general for low M , an increase of turbulence intensity (M_t) leads to stronger shocks ($R_\rho(M, M_t) > 0$) relative to RH, or equivalently a shock in a uniform laminar flow at the same M . However, as M increases $R_\rho(M, M_t)$ changes sign and jumps become weaker. At higher M , $R_\rho(M, M_t)$ decrease monotonically towards zero from below indicating a vanishing turbulence effect as $M \rightarrow \infty$. A similar general behaviour is observed for the similarly defined $R_p(M, M_t)$ and $R_T(M, M_t)$ shown in figure 11.

Two characteristic Mach numbers can now be identified for $R_\rho(M, M_t)$. First, $M_{cr}^\rho(M_t)$ is the critical Mach number at which $R_\rho(M, M_t)$ changes sign. This can be readily found by solving $R_\rho(M, M_t) = 0$ numerically for fixed M_t . The result is shown in figure 12(a) along with the critical Mach numbers for pressure and temperature. We see that, while qualitatively similar, the critical Mach number is numerically different for ρ , p and T . Conditions below and above the corresponding $M_{cr}(M_t)$ lines represent stronger and weaker shock jumps respectively for the different thermodynamic variables. We can also see that the critical Mach number appears mainly in the broken regime.

An interesting prediction by the theory is the existence of conditions at which pressure and density jumps are weakened by turbulence ($M > M_{cr}^\rho$ and $M > M_{cr}^p$) while temperature jumps are strengthened ($M < M_{cr}^T$). This is indeed supported by our DNS data at $M_t = 0.39$ and $M = 1.2$ where temperature experiences an increase stronger than RH while pressure and density experience a weaker-than-RH increase across the shock. This is seen in figure 13(a) where we plot DNS data for this case along with corresponding RH jumps. In figure 13(b) we show a condition where all thermodynamic variables experience a stronger-than-RH jump due to turbulence.

A second characteristic Mach number is the location of the minimum observed for given M_t in figure 11. This corresponds to the condition at which the largest turbulent effects are observed, and are denoted by $M_m^\rho(M_t)$, $M_m^p(M_t)$ and $M_m^T(M_t)$ for density, pressure and temperature, respectively. These can be obtained by solving

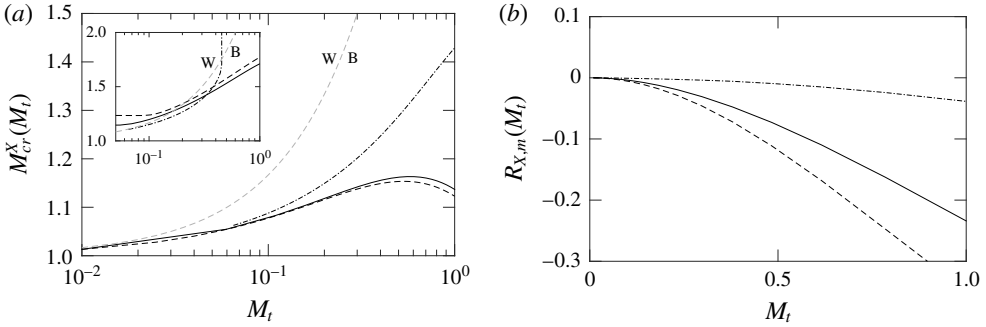


FIGURE 12. (a) Critical Mach numbers ($M_{cr}^X(M_t)$) for density ($X = \rho$, solid), pressure ($X = p$, dashed) and temperature ($X = T$, dash-dotted). Grey dashed line at $M_t/\Delta M = 0.6$ separates the wrinkled (W) and broken (B) regimes. (b) Maximum weakening of shock jumps due to turbulence measured as the maximum relative departure from RH relations for density ($X = \rho$, solid), pressure ($X = p$, dashed) and temperature ($X = T$, dash-dotted) for a given M_t .

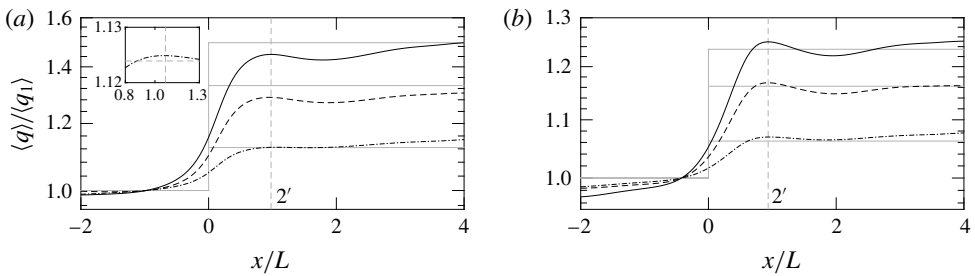


FIGURE 13. Variation of normalized pressure (solid, $q = p$), density (dashed, $q = \rho$) and temperature (dash-dotted, $q = T$) across the shock. (a) $(M, M_t, R_\lambda) \approx (1.2, 0.39, 13)$ which corresponds to $M < M_{cr}^T$ and $M > M_{cr}^p, M_{cr}^\rho$. Inset: detailed view of temperature around x_2' . (b) $(M, M_t, R_\lambda) \approx (1.1, 0.29, 10)$ which corresponds to $M < M_{cr}^T, M_{cr}^p, M_{cr}^\rho$. Grey solid lines represent the laminar inviscid limits. Vertical grey dashed lines indicate the location of x_2' .

$\partial R_\rho(M, M_t)/\partial M = 0$ and similar equations for density and pressure. The result is shown in the inset of figure 12(a). $M_m(M_t)$ also is mainly in the broken regime though the three thermodynamic quantities lie close to each other and to the WB line. However, for higher M_t we see $M_m^T(M_t)$ grows substantially indicating that the strongest turbulence effect on temperature moves to higher values of M .

The analysis here also suggests that, for a fixed M_t , there is a bound on how much a shock can be weakened by turbulence. This is given by the minimum value of $R_\rho(M, M_t)$ ($R_{\rho,m}$ for short), which occurs at the second characteristic Mach number, that is $R_{\rho,m} \equiv R_\rho(M_m^p(M_t), M_t)$. This quantity is shown in figure 12(b) where we see that pressure jumps can be of the order of 30% weaker at high M_t . Weakening of temperature jumps however, are much smaller, staying below ~5% for the Mach numbers studied here. The Mach number at which this maximum effect is realized can be obtained from figure 11 or the full analytical expressions.

3.2.3. Entropy

Finally we turn to entropy which is also expected to contain both laminar and turbulent contributions. As before, one use QE to obtain the mean entropy jump across

a shock as:

$$\langle \Delta s \rangle = \langle \Delta s^{\leq} \rangle^{\leq} + \langle \Delta s^{\geq} \rangle^{\geq}. \quad (3.18)$$

For supersonic regions, the standard entropy jump is $C_p \ln(T_2'/T_1) - R \ln(p_2'/p_1)$ which can also be written as

$$\Delta s^{\geq} = C_p (\ln T_2' - \ln T_1) - R (\ln p_2' - \ln p_1). \quad (3.19)$$

The different terms can be computed as before. For example, the logarithm of the instantaneous temperature in terms of M and m is

$$\ln T_1 = \ln \left(\left[\frac{\gamma - 1}{2} (M + m)^2 + 1 \right]^{-1} T_{01} \right), \quad (3.20)$$

which upon expanding in Taylor series and averaging leads to:

$$\begin{aligned} \langle \ln T_1 \rangle^{\geq} &= \ln(M^{-1}) \langle m^0 \rangle^{\geq} - \frac{2(\gamma - 1)M}{(\gamma - 1)M^2 + 2} \langle m \rangle^{\geq} \\ &+ \frac{(\gamma - 1)[(\gamma - 1)M^2 - 2]}{[(\gamma - 1)M^2 + 2]^2} \langle m^2 \rangle^{\geq} + \ln T_{01} \langle m^0 \rangle^{\geq}. \end{aligned} \quad (3.21)$$

We can similarly obtain $\langle \ln T_2' \rangle^{\geq}$, $\langle \ln p_1 \rangle^{\geq}$ and $\langle \ln p_2' \rangle^{\geq}$.

For subsonic regions where there is no shock, the entropy increase will be solely due to the dissipative nature of turbulence. Obukhov (1949) showed that entropy generation due to turbulent fluctuations in temperature is proportional to the temperature variance. Specifically he showed that when the flow decays from a state characterized by a temperature variance $\langle T'^2 \rangle$, the total entropy increase is $\langle \Delta s \rangle \approx C_p \langle T'^2 \rangle / \langle T \rangle^2$. In the present case, turbulence will not be completely dissipated as it crosses the shock region and reaches x_2' . However, it is still expected that the entropy increase will be proportional to the variance of temperature of the incoming flow. Furthermore, this variance can be written in terms of the turbulent Mach number as $\langle T'^2 \rangle / \langle T \rangle^2 \approx (A^2/9)(\gamma - 1)^2 M_t^4$ (Donzis & Jagannathan 2013). Thus, for holes one can expect

$$\Delta s^{\leq} = \alpha_s C_p (\gamma - 1)^2 M_t^4, \quad (3.22)$$

where all prefactors are absorbed in the constant α_s .

Finally, with (3.19) and (3.22) we take the conditional averages for the two regions as in (3.18) to obtain

$$\frac{\langle \Delta s \rangle}{C_p} = g_s(M, M_t). \quad (3.23)$$

The final expressions that comprise the function $g_s(M, M_t)$ are explicitly shown in appendix A.

The DNS data of entropy jump across the shock along with the theoretical prediction (3.23) are shown in figure 14. The comparison shows good agreement though there is some scatter in the data. At very low M_t , the change of entropy is due entirely to the well-known laminar jumps (Thompson 1984). As M_t increases, we see a substantial increase in entropy production in both DNS data and the theoretical prediction (3.23).

The theoretical result approaches an asymptotic M_t^4 at high M_t indicating that turbulence entropy generation becomes the dominant contribution. Note that the

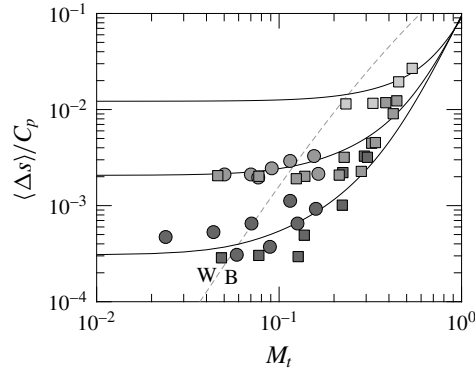


FIGURE 14. Mean entropy increase from IT (■) and SDT (●) simulations. Solid lines correspond to the analytical solution (3.23) at $M = 1.1, 1.2,$ and 1.4 (bottom to top) with $\alpha_s = 1.176$. Grey dashed line at $M_t/\Delta M = 0.6$ separates the wrinkled (W) and broken (B) regimes.

supersonic regions also contains ‘turbulence effects’: this is seen, for example, from the second term in (3.21) which vanishes as the incoming flow fluctuations weakens ($M_t \rightarrow 0$). However, the asymptotic behaviour of these terms is a weaker power law than M_t^4 . Furthermore, the entropy increase through shock holes is independent of the mean Mach number as it only reflects entropy production due to turbulent dissipation. Thus, the observed decreasing gap between curves at different M as M_t increases is also supportive of an increasingly dominant contribution from turbulent decay.

3.2.4. Remarks

We conclude this section with a few remarks about the generality of the results above. First, we note that there is a negligible Reynolds number effect for mean jumps. This is not unexpected since RH jumps can be shown to be the same in viscous or inviscid flows – molecular transport properties (viscosity and thermal conductivity) only determine the structure of the shock (Zeldovich & Raizer 2002). Thus, the sole dependence on M and M_t in (3.14)–(3.16) is indeed a very general form, under QE, for jumps. Second, we note that there is little difference between jumps in isotropic and anisotropic turbulence. This suggests that the QE assumption, based on locally one-dimensional shock, does provide an accurate description even with relatively strong turbulence. Finally, we stress that conclusions here result from calculating quantities at x_2' which can be argued to be still unaffected by turbulent mixing downstream of the shock. At x_2 , however, quantities are expected to be affected by turbulence processes and, indeed, Reynolds number effects have been observable (Andreopoulos *et al.* 2000; Donzis 2012a). These observations are consistent with separate regions, one where the flow is dominated by ‘shock effects’ ($x < x_2'$), and another one where it is dominated by ‘turbulence effects’ ($x > x_2$). The region $x_2' < x < x_2$ can then be thought of as a transition region where the fully developed incoming turbulence has been deeply distorted by the shock and is evolving towards its fully developed state. Although our data support this picture, it is unclear to what degree actual flows consist of ‘pure’ regions dominated exclusively by one of these processes. Detailed investigations of this conceptual picture and the relative dominance of different process in each region are worth pursuing, but beyond the objectives here.

3.3. Shock structure

The effects of turbulence on shock characteristics have been studied theoretically in the literature (Ribner 1954*a,b*; Williams & Howe 1973; Zank *et al.* 2002; Wouchuk, de Lira & Velikovich 2009) and observed experimentally (Hesselink & Sturtevant 1988) and numerically (Lee *et al.* 1993; Larsson & Lele 2009). These investigations helped identify two regimes – wrinkled and broken – which result from different levels of turbulence intensity. The former corresponds to an interaction in which the shock retains its structure as a sharp gradient over a weakly modified uniform shock plane. The latter corresponds to a strongly modified shock plane with ‘holes’ through which properties may change smoothly or have multiple peaks (Hesselink & Sturtevant 1988; Lee *et al.* 1993).

A quantitative metric that has been used to characterize inhomogeneities in the structure of the shock is the r.m.s.-to-mean dilatation at the shock (Lee *et al.* 1993; Larsson & Lele 2009)

$$\Theta = \left(\frac{\langle \theta_s^2 \rangle_s}{\langle \theta_s \rangle_s^2} - 1 \right)^{1/2}, \quad (3.24)$$

where θ_s is the dilatation at the shock location which is identified as the largest negative value of dilatation along the streamwise direction x for a given location (y, z) . That is, $\theta_s(y, z) = \min_x \theta(x, y, z)$. Note that since the location where θ attains its minimum is, in general, different for different locations (y, z) , the averages in (3.24) are not over planes at fixed x , but instead over all $\theta_s(y, z)$ – we use the additional subscript s in $\langle \cdot \rangle_s$, to differentiate it from plane averages $\langle \cdot \rangle$. DNS data presented below are also time averaged.

Following Donzis (2012*b*), one can write the maximum negative dilatation at the shock as $\theta_s \approx \llbracket u \rrbracket / \delta_t$ where $\llbracket u \rrbracket$ is the velocity change across the shock and δ_t the shock thickness which, to leading order, can be written as $(\rho c / \mu) \llbracket u \rrbracket (\Delta M + m)$. Using unconditional averages over the entire surface and assuming $\llbracket u \rrbracket$ is, to leading order, not affected by fluctuations, QE leads to $\langle \theta_s \rangle_s \sim (\langle \rho_1 \rangle \langle c_1 \rangle / \langle \mu_1 \rangle) \llbracket u \rrbracket \Delta M$ and $\langle \theta_s^2 \rangle_s \sim (\langle \rho_1 \rangle \langle c_1 \rangle / \langle \mu_1 \rangle)^2 \llbracket u \rrbracket^2 (\Delta M^2 + M_t^2 / 3)$ which, when used in (3.24), leads to:

$$\Theta \approx \frac{1}{\sqrt{3}} \frac{M_t}{\Delta M}. \quad (3.25)$$

This has been shown to provide good collapse of the existing data (Donzis 2012*b*; Boukharfane, Bouali & Mura 2018). However, equation (3.25) is expected to be accurate only when turbulence is relatively weak. This is indeed the case as seen in figure 15, where we show Θ for the present data (in colour) along with other existing data. The dash-dotted line is (3.25) while the solid line contains the next-order term in the expansion (Donzis 2012*b*), that is $\Theta \approx e_1 M_t / \Delta M + e_2 (M_t / \Delta M)^3$ where e_1 and e_2 are fitting constants. There is good agreement between the data and the theory in the wrinkled regime ($M_t / \Delta M \lesssim 0.6$) consistent with previous studies (Donzis 2012*b*; Boukharfane *et al.* 2018).

As $M_t / \Delta M$ increases, however, departures are apparent with two interesting features. First we see that, in spite of significant scatter, Θ seems to approach an asymptotic value (Θ_∞) at high $M_t / \Delta M$ with a value dependent on the Reynolds number. Second, DNS data depart from the QE prediction at higher $M_t / \Delta M$ when R_λ is high. This effect does not appear to be due to the increase of holes in the shock since figure 7 shows that the fraction of subsonic regions does not depend on R_λ . A potential explanation for this effect is that at low R_λ , stronger viscous effects

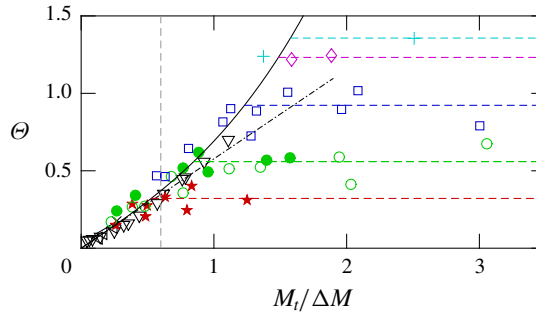


FIGURE 15. (Colour online) R.m.s.-to-mean dilatation at the shock for $R_\lambda \approx 5$ (red stars), $R_\lambda \approx 10$ (green circles), $R_\lambda \approx 25$ (blue squares), $R_\lambda \approx 45$ (magenta diamonds), $R_\lambda \approx 65$ (cyan pluses). Open and closed symbols are for IT and SDT simulations, respectively. Vertical grey dashed line at $M_t/\Delta M = 0.6$ for reference. Horizontal dashed lines: average of DNS data at high $M_t/\Delta M$ for $R_\lambda \approx 5, 10, 25, 45$ and 65 from bottom to top. Other symbols: Jamme *et al.* (2002) (\times), Larsson & Lele (2009) (∇) and Boukharfane *et al.* (2018) (\triangleleft).

enhance transverse diffusion of momentum which would make the one-dimensional local behaviour assumption in QE less applicable. However, a thorough verification of this explanation requires more data at a wide range of parameters.

Before we discuss the asymptotic value Θ_∞ , it is instructive to see the structure of the flow as it crosses the shock. In figure 16 we show, for three different cases, plane-averaged dilatation along the streamwise direction (dark line) with a set of instantaneous dilatation profiles at some arbitrary locations (light grey lines). In (a) we show a wrinkled case (though close to broken limit) with a very strong mean dilatation comprised of similar instantaneous profiles. At higher $M_t/\Delta M$ in the broken regime (b) we also see a strong peak though spatially broader, consistent with theoretical predictions (Donzis 2012b). Individual dilatation profiles, however, display a wider range of behaviours: some have the same qualitative peak while others present multiple peaks or a very broad smooth variation (Lee *et al.* 1993; Larsson & Lele 2009). At even higher values of $M_t/\Delta M$ (c) individual profiles show very large fluctuations upstream and downstream of the shock comparable to the mean (dark line). It is interesting to note that while fluctuations in this case are of the same order as the mean, the latter still shows the same peak as, although much broader than, in the wrinkled regime.

Typical distributions of Reynolds stresses and mean pressure are shown in figure 17 at similar conditions. In (a) and (b) we see that, consistent with observations in the literature, the downstream peak of R_{11} at x_2 decreases with M_t . As M_t increases further, we observe both the peaks upstream and downstream of the shock (x_1 and x_2 , respectively) vanish. We term this, then, the ‘vanished’ regime. Clearly in this regime, it is not possible to compute amplification factors since no upstream and downstream locations can be identified unambiguously as Reynolds stresses undergo a classical turbulent decay. It is interesting that other mean quantities such as mean pressure (c,d) or mean velocity retain the typical qualitative behaviour of a shock. While these mean gradients may lead to production by mean shear in the Reynolds stress budget, because of the short residence time within the shock region, they cannot, on average, counteract the viscous decay.

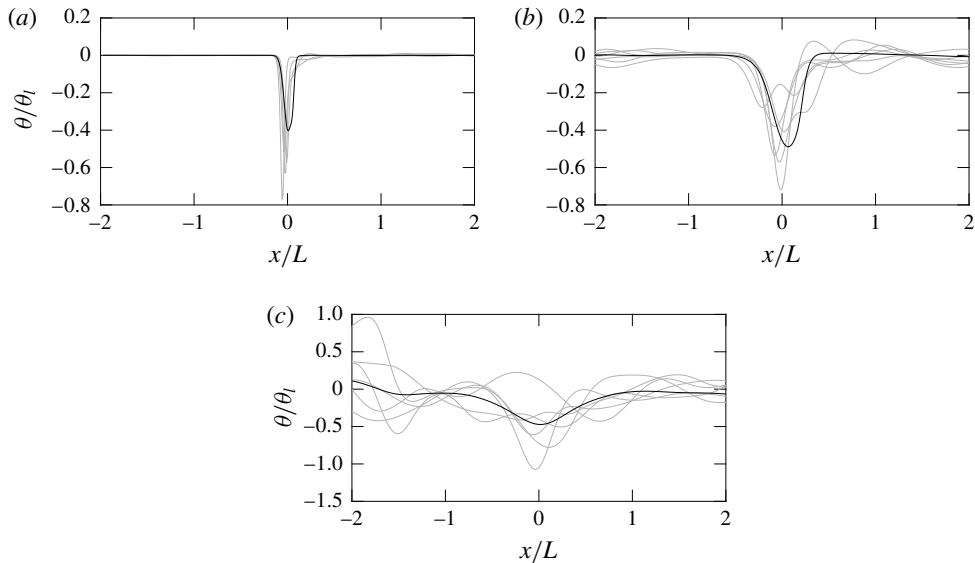


FIGURE 16. Instantaneous dilatation normalized by laminar condition (θ_l) along the streamwise direction at different transverse locations (grey) and their mean (black) at $M = 1.1$, $R_\lambda \approx 10$ and (a) $M_t = 0.05$ (wrinkled), (b) $M_t = 0.14$ (broken) and (c) $M_t = 0.34$ (vanished).

Furthermore, since in the vanished regime no x_1 location can be identified, it is also not possible to determine R_λ , M_t or ΔM upstream of the shock. Alternatively, one can estimate them by assessing the limit at which local extrema vanish for R_{11} . For example, for $R_\lambda \approx 5$, 10 and 25, we find that the vanished regime appears at $M_t/\Delta M \approx 2.14$, 3.4 and 4.4, respectively. In these three cases, K is found to be very close to 1.0. This is, in fact, not unexpected. As we show below, the amplification factor for R_{11} shows a universal behaviour with K for relatively high K . In particular, it decreases with K and reaches values around 0.8 at $K \approx 1$. Beyond this value of K no local extrema are observed and amplification factors cannot be obtained.

We now get back to the asymptotic value Θ_∞ . As $M_t/\Delta M$ increases, increasingly large areas of the shock are subsonic and present holes. However, it is unclear what the value of θ_s is across holes. Furthermore, as turbulence becomes more intense, the flow will experience stronger locally three-dimensional effects which will favour strong mixing in all directions and thus weaken the applicability of QE. According to the definition of Θ one searches for the largest negative dilatation around the location of the shock along x for a given (y, z) location. When turbulence is strong (see instantaneous profiles in figure 16c), one would expect Θ to be essentially dominated by turbulence statistics and we can then use known scaling laws for velocity gradients. However, Θ is based on the average of the minimum dilatation close to the average location of the shock. While the mean dilatation in isotropic turbulence is zero, the average of minimum dilatation across an arbitrary plane is not. Thus, we make the additional assumption that these values are, to first approximation, proportional to the average magnitude of those gradients. Moments of velocity gradients are known to scale as power laws with the Reynolds number (Monin & Yaglom 1975): $\langle |\partial u/\partial x|^n \rangle = C_n (u_{1,rms}/L)^n R_\lambda^{2d_n}$ where C_n are flow-dependent constants and d_n are the so-called scaling exponents. While these power laws have

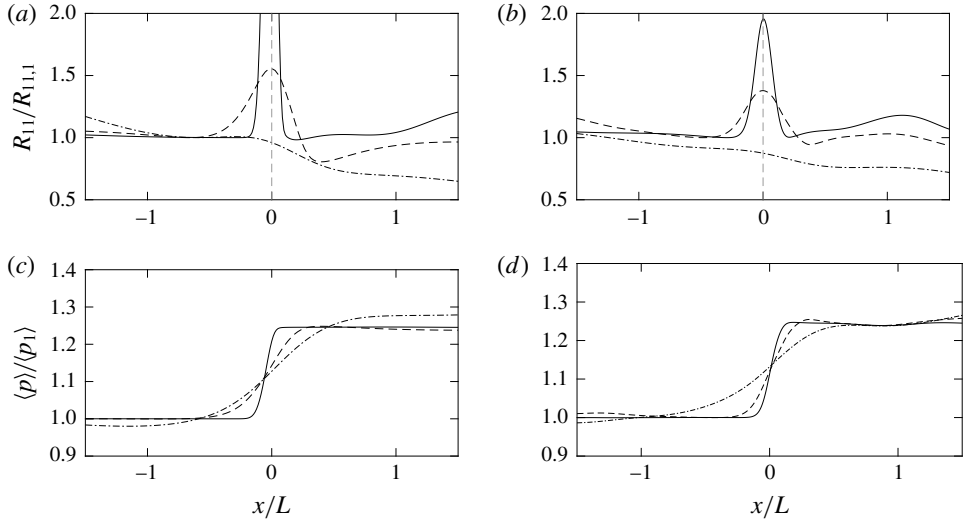


FIGURE 17. Distributions of R_{11} at $M = 1.1$, (a) $R_\lambda \approx 10$ and $M_t = 0.05$ (solid), $M_t = 0.14$ (dashed) and $M_t = 0.34$ (dash-dotted) and (b) $R_\lambda \approx 25$ and $M_t = 0.22$ (solid), $M_t = 0.3$ (dashed) and $M_t = 0.44$ (dash-dotted). Distribution of p at (c) $R_\lambda \approx 10$ and $M_t = 0.05$ (solid), $M_t = 0.14$ (dashed) and $M_t = 0.34$ (dash-dotted) and (d) $R_\lambda \approx 25$ and $M_t = 0.22$ (solid), $M_t = 0.3$ (dashed) and $M_t = 0.44$ (dash-dotted).

been historically believed to hold only for high Reynolds numbers, recent work suggests that their applicability extends to rather low Reynolds numbers (Schumacher, Sreenivasan & Yakhot 2007; Schumacher *et al.* 2014; Yakhot & Donzis 2017). We then estimate Θ_∞ , when turbulence dominates, as

$$\Theta_\infty \approx \left(\frac{\langle |\partial u / \partial x|^2 \rangle}{\langle |\partial u / \partial x|^2 \rangle} - 1 \right)^{1/2} \approx c_1 (c_2 R_\lambda^{2(d_2 - 2d_1)} - 1)^{1/2}, \quad (3.26)$$

where all order-unity prefactors have been absorbed in the constants c_1 and c_2 . The exponents have been studied extensively and are relatively well known (e.g. Schumacher *et al.* 2007; Yakhot & Donzis 2018) with values $d_2 = 1$ and $d_1 = 0.46$.

In figure 18 we show Θ_∞ from DNS along with (3.26) with $c_1 = 1.756$ and $c_2 = 0.8217$ obtained as best-fit coefficients indeed of order unity. The good agreement between theory and DNS supports the idea of Θ being dominated by turbulence rather than the shock at those conditions. At the same time from figure 7 we see that even for $M_t / \Delta M \approx 3$ the subsonic regions are only approximately 30% of the shock area. Thus, the dominance of turbulence appears to stem from strong turbulent mixing across and after the weak shock.

4. Amplification factors

As we have shown, turbulent flows can significantly affect jumps in thermodynamic variables as well as statistical features of the shock structure. Simultaneously, the occurrence of a shock also affects the characteristics of turbulent flows. A useful quantity to characterize these changes is the so-called amplification factor, $G \equiv R_{11,2} / R_{11,1}$. The main rationale behind selecting x_2 as the downstream location

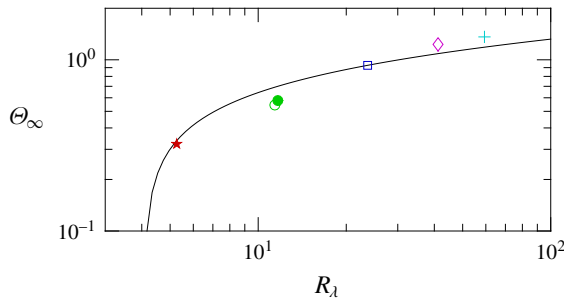


FIGURE 18. (Colour online) Asymptotic value of Θ as a function of R_λ . Different symbols represent the average of DNS data at a fixed R_λ in the asymptotic state (see text). Symbols as in figure 15. Solid line is (3.26) with $c_1 = 1.756$ and $c_2 = 0.8217$.

(Donzis 2012a and references therein; Ryu & Livescu 2014; Boukharfane *et al.* 2018) is that, as discussed in § 2.3, the flow undergoes a viscous decay beyond that location where inviscid assumptions are less justified. Here we follow this convention and use x_2 . We note, however, that other methods have also been proposed (e.g. Larsson & Lele 2009, where Reynolds stresses are extrapolated to the mean shock location in an attempt to account for the viscous decay).

When data available in the literature are examined collectively, it is clear that G depends not only on M (as predicted by LIA) but also on the turbulent Mach number and the Reynolds number (Andreopoulos *et al.* 2000; Donzis 2012a). In Donzis (2012a) we proposed an alternative parameter to characterize the interaction (K) defined as

$$K \equiv \delta_i / \eta, \quad (4.1)$$

where δ_i is the shock thickness at a uniform Mach number, M . As K decreases, the shock becomes increasingly smaller relative to turbulence scales. One would, then, expect the interaction to approach the conditions in which LIA is applicable, that is when the shock is a discontinuity interacting with very weak fluctuations in an inviscid flow (low M_t and high R_λ). Indeed, recent well-resolved simulations (Ryu & Livescu 2014) support this limiting expectation. Our interest here, however, is in the case of finite M_t and R_λ where both parameters play a role. Using classical scaling arguments, one can also write $K = M_t / R_\lambda^{1/2} \Delta M$ (Donzis 2012a), an expression that was also used in other contexts to assess resolution in DNS (Moin & Mahesh 1998).

Figure 19 shows the amplification factor for all the DNS database presented here (in colour) along with other amplification factors in the literature. In (a) we show G as a function of ΔM , the only parameter that controls the interaction within LIA. Wide differences are seen between the LIA prediction (solid line) and data. As pointed out before (Donzis 2012a) these departures are systematic in R_λ and M_t but disappear when data are plotted against K . This is shown in figure 19(b) where we see a high degree of collapse of the new and earlier data onto a single curve at high K which is well represented by a power law of the form $G \approx 0.75K^{-1/4}$ proposed in Donzis (2012a). As pointed out above, as $K \rightarrow 0$, we have $\delta_i \ll \eta$ and one expects to recover conditions in which LIA applies. Ryu & Livescu (2014) indeed observed this trend. Thus, data suggest a universal behaviour of amplification factors with K , with a Mach-number-dependent asymptotic state as $K \rightarrow 0$. At high K , the amplification factor is seen to go below unity, a possibility suggested before (Donzis 2012a),

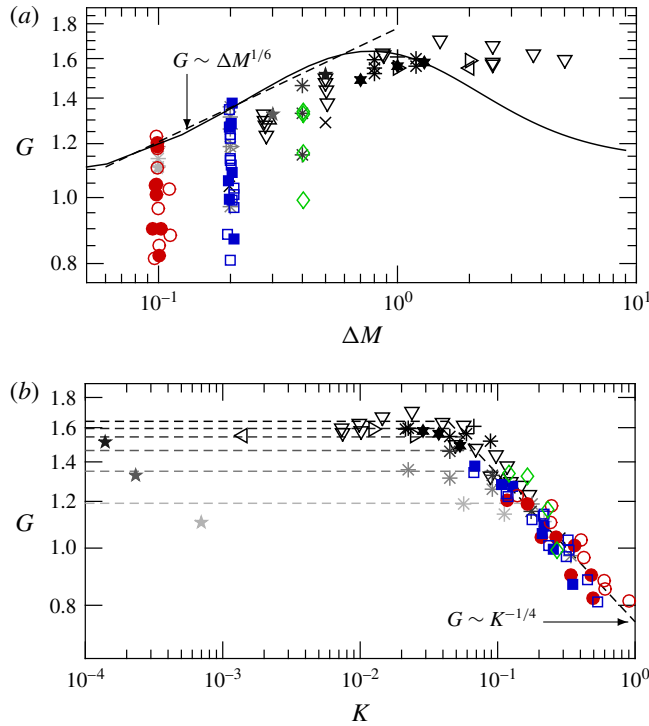


FIGURE 19. (Colour online) (a) Collection of amplification factors of streamwise velocity as a function of ΔM along with LIA prediction (Ribner 1954b). (b) Same data as a function of $K = M_t / (R_\lambda^{1/2} \Delta M)$. Horizontal dashed lines: LIA prediction for $M = 1.1, 1.2, 1.3, 1.4, 1.5$ and 1.8 from bottom to top. In both panels red circles correspond to $M = 1.1$, blue squares to $M = 1.2$ and green diamonds to $M = 1.4$. Open and closed symbols are for IT and SDT simulations, respectively. Other symbols: Lee *et al.* (1993, 1997) (\triangleright), Hannappel & Friedrich (1995) (+), Barre *et al.* (1996) (\triangleleft), Mahesh *et al.* (1997) (Δ), Jamme *et al.* (2002) (\times), Larsson & Lele (2009) and Larsson *et al.* (2013) (∇), Ryu & Livescu (2014) (*, grey levels for $M = 1.1, M = 1.2$ and $M = 1.4$ from light to dark), Boukharfane *et al.* (2018) (\star) and Tanaka *et al.* (2018) (\star , grey levels for $M = 1.1, M = 1.3$ and $M = 1.5$ from light to dark).

which represents turbulence attenuation as it crosses the shock. Beyond $K \approx 1.0$, amplification factors cannot be defined as the extrema at x_1 and x_2 vanish, marking the beginning of the vanished regime.

This transition between scaling laws based on different non-dimensional groups in particular limits is observed in diverse physical phenomena from equations of states near the critical point (Widom 1965) to flows in rough pipes (Goldenfeld 2006). In the latter, Goldenfeld studied the transition from the well-known power-law dependence of the friction coefficient on the Reynolds number to a Reynolds-number-independent scaling law on the ratio of roughness to pipe diameter. In such cases, the dependence on two parameters can be cast in terms of a reduced parameter under which data are observed to collapse into a single universal curve. The data in figure 19(b) are very suggestive of such a behaviour with a transition from K to M as $K \rightarrow 0$. Thus we start by considering the general relation $G = f_1(K, \Delta M)$ for some unknown function f_1 and its observed limiting behaviour. At high values of K we observe a $K^{-1/4}$ scaling;

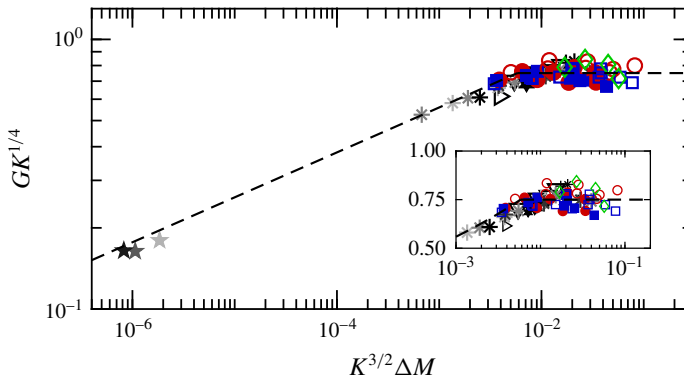


FIGURE 20. (Colour online) Universality of amplification factor based on the scaling (4.3) for data with $M < 2$. Same colours and symbols as in figure 19. Inset: detailed view of plateau with linear scale in the vertical axis.

at low values of K , G tends to LIA. Note that this imposes significant constraints on the functional form for f_1 . For simplicity in the analysis we consider the behaviour for $M \lesssim 2$ where the LIA solution can be approximated as a power law of the form $\Delta M^{1/6}$ as shown in figure 19(a) with a dashed line. Following Widom (1965), we propose the following scaling relation:

$$G = K^{-1/4} f_2(K^\alpha \Delta M), \quad (4.2)$$

where α is an exponent to be determined by specific limits. Note that this is essentially a case of incomplete similarity also justified from renormalization group theory (Barenblatt 2003) where universality is revealed only under a suitable combination of the original governing non-dimensional parameters, although this combination cannot be obtained on dimensional grounds alone. Consistency with the $\Delta M^{1/6}$ asymptotic behaviour requires that $f_2(x) \sim x^{1/6}$ as $x \rightarrow 0$ and, simultaneously, that the K dependency must disappear. It is easy to see that G will become independent of K in that limit if $\alpha = 3/2$. The final result is then

$$G = K^{-1/4} f_2(K^{3/2} \Delta M). \quad (4.3)$$

The implication of this scaling is that while the phenomenon depends on the two parameters K and ΔM at two different limiting conditions, a collapse on a universal curve will emerge if one plots $G/K^{-1/4}$ as a function of $K^{3/2} \Delta M$. This is indeed the case as seen in figure 20 where we show data at $M < 2$, the condition at which the scaling argument applies. We can see that, for example, the data from Ryu & Livescu (2014) which depart from K scaling at different ΔM (figure 19b) collapse onto the line with a slope of $1/6$. This low K behaviour is readily understood by recalling that $f_2(x) \sim x^{1/6}$ at small x which corresponds to $G \sim \Delta M^{1/6}$. At high K , $G \sim K^{-1/4}$ which under the normalization in the plot is seen as a horizontal line. Given the number and variety of data sources and flow conditions collected here, combined with the lack of systematic trends with Reynolds, turbulent and mean Mach numbers individually, the collapse of the data is deemed very satisfactory. This is especially so when one compares with figure 19(a) where the scatter around the theoretical prediction is reduced by a factor of 3 and, more importantly, no systematic trends with R_λ and M_t are observed.

The transition from K -scaling to M -scaling allows us also to determine the combination of parameters at which it occurs. From figure 20, we observe that this transition happens at $K^{3/2}\Delta M \approx 0.0055$. Explicitly, we can then write

$$K_{tr} \approx \frac{0.03}{\Delta M^{2/3}}, \quad (4.4)$$

which is found to be consistent with the data in figure 19(b), especially those of Ryu & Livescu (2014) which clearly show the transition. We also point out that (4.4) provides a precise meaning to the distinction between low- K and high- K interactions, a classification that was put forth only in qualitative terms (Donzis 2012a): amplification factors at $K < K_{tr}$ could be well represented by LIA; amplification factors at $K > K_{tr}$ scale as $G \approx 0.75K^{-1/4}$. Equation (4.4) can also be written as $(\delta_l/\eta)_{tr} \approx 0.03/\Delta M^{2/3}$ which emphasizes the fact that the transition depends not only on the ratio of length scales. From figure 20 we see that the majority of the data in the literature with $M < 2$ correspond to high- K interactions.

We close this section by noting that the amplification factor shows no systematic difference between the two types of mechanisms used to generate turbulence here, namely, IT and SDT (§ 2.2). Since the former is statistically isotropic while the latter is not with longitudinal stresses R_{11} up to 64% larger than transverse stresses R_{22} (table 2), data suggest that amplification of turbulence in the streamwise direction may be dominated by one-dimensional processes in that direction. This is consistent with the discussion in § 3.2 where it was argued that the dynamics in the region upstream of x_2 is mainly determined by shock effects in QE. Fully developed turbulence, on the other hand, is attained only at x_2 beyond which well-known return-to-isotropy processes (not accounted for in LIA) are expected to operate at relatively long time scales (Larsson & Lele 2009; Larsson *et al.* 2013; Ryu & Livescu 2014; Livescu & Ryu 2016). In light of these observations, it may not be entirely surprising the virtually undetectable dependence of G on anisotropy in the incoming turbulence.

5. Summary and conclusions

We have investigated the interaction of a normal shock and turbulence with a focus on high intensity turbulence levels. We presented theoretical results on turbulent jumps of mean thermodynamic quantities, shock structure and amplification factors, all supported by a large database of new high-resolution shock-resolving DNS at a wide range of M_t (0.02 – 0.54) and R_λ (5 – 65), and mean Mach numbers, M , up to 1.4.

A number of theoretical results were presented using the quasi-equilibrium assumption (Donzis 2012b). Under such an assumption, the shock responds instantaneously to local changes in upstream conditions due to turbulent fluctuations. When turbulent fluctuations are strong enough, the flow can become subsonic locally. In Donzis (2012b) we proposed this to be the origin of so-called holes in the shock, a situation commonly referred to as the broken regime of the interaction which emerges when $M_t/\Delta M \gtrsim 0.6$. Here we presented DNS data that quantitatively support the assertion that beyond this threshold subsonic regions become rapidly apparent, leading to a broken regime.

We presented analytical expressions for mean jumps across the shock using the QE approximation, in which standard RH jumps are valid locally. The resulting functions depend on both M and M_t compared to RH jumps which depend solely on M . Our and others' numerical data agree well with the theoretical predictions

and we argued that while R_λ does not appear in the final expressions, this can be justified from analysis of the governing equations in the one-dimensional limit. The effect of anisotropy on the incoming turbulence was found to be negligible on mean jumps, again supporting the basic tenets behind QE. The analytical results apply well both in the wrinkled and broken regime due to the different treatment of supersonic and subsonic regions ahead of the shock. Interestingly, though, departures from RH jumps of mean variables are seen even in the wrinkled regime due to the nonlinear functional form of RH jumps which, when averaged, result in values different than RH jumps using mean properties ahead of the shock. Note that this effect is missing when linearized RH jumps are used in theories such as LIA. Furthermore, in the latter, mean properties are considered known boundary conditions to the problem at the mean Mach number M . Our results, consistent with other DNS in the literature, do not support this assumption which may be, in part, responsible for LIA being unable to capture the observed behaviour beyond weak fluctuations. This change in mean properties has also relevance for practical applications where shock stabilization in a turbulent environment is critical such as flows in supersonic nozzles or in scramjet engines. It can also provide guidance in designing stationary STI experiments and simulations as an incorrect back pressure will lead to drifting shocks.

The theoretical results were further found to provide quantitative predictive capabilities. For example, we found that turbulence can weaken (as argued before) but also strengthen jumps depending on a critical Mach number M_{cr} defined here which in turns depend on the intensity of turbulent fluctuations through M_t . For $M < M_{cr}$, jumps are stronger than in laminar flows at the same M ; for $M > M_{cr}$ jumps are weaker. Furthermore, density, pressure and temperature present different critical Mach numbers giving raise to conditions in which temperature jumps are larger than RH while density and pressure jumps are weaker than RH. These predictions have been verified with DNS data.

Thus we conclude that collectively the data support QE as a good approximation which leads to analytical results for density, pressure, temperature and entropy, consistent with the available data. In fact, it is interesting to observe how well it performs even with highly broken shocks where three-dimensional effects could play a role. We also note that QE is not expected to be accurate for variables at locations beyond x_2' where turbulent – as opposed to shock – processes dominate the dynamics. It is also unclear whether derivations under QE are applicable to, e.g. variances of thermodynamic quantities. This is part of ongoing efforts.

The effect of turbulence on the shock structure was quantified with the r.m.s.-to-mean dilatation at the shock, Θ , suggested previously in the literature. Under QE, Θ is found to depend, in the wrinkled regime, on the non-dimensional group $M_t/\Delta M$ where the theory agrees well with the present DNS as well as other DNS in the literature. Departures from the theory are seen for $M_t/\Delta M \gtrsim 0.6$ where stronger turbulent effects create increasingly large areas with holes. At high $M_t/\Delta M$, an asymptotic value of Θ is observed which depends on the Reynolds number. This was explained by the fact that at high turbulence intensities, dilatation fluctuations are dominated by turbulent effects. Thus, classical results on turbulence gradients were used to obtain Θ which agrees with DNS data.

Finally, we presented results on turbulence amplification due to the shock. The focus was on G , the amplification factor of the streamwise velocity component. A large collection of results, mainly from simulations, was presented. The new simulations presented here cover a wide range of parameters and extended the results in the literature to interactions at relatively high K . The large amount of data

collected exhibit large departures from LIA which are found to depend systematically on M_t and R_λ . Consistent with Donzis (2012a) new data exhibit a collapse on a single curve when plotted against K for high K . However, as pointed out in Ryu & Livescu (2014) at low K , the asymptotic behaviour depends on M , consistent with LIA. This dependence on two parameters in two different limits resembles Widom scaling in critical phenomena. Here, its application leads to universality of the form $GK^{1/4} = f_2(K^{3/2} \Delta M)$ which collapses all the data with no systematic trend observed in any other governing parameter. This led to a transition criterion ($K_{tr} \approx 0.03/\Delta M^{2/3}$) between low- K and high- K interactions which separates interactions where LIA applies and when $G \sim K^{-1/4}$ applies, respectively. The successful characterization of departures from LIA, provides an opportunity for generalizations of LIA and other theories, which can now use the correct scaling behaviour presented here as a constraint. Modifications would likely be required to generalize results here to more complex geometries such as shock–boundary layer interactions, but are of clear interest.

In summary, the canonical interaction of a normal shock with high-intensity turbulence was studied theoretically and numerically. A theory was proposed which captures turbulence effects on jumps across the shock as well as the structure of the shock surface. The theory also predicts new regimes of the interaction (e.g. vanished regime, attenuation or amplification of mean jumps) which are supported quantitatively by numerical data. Finally, new universal scaling laws were proposed for amplification factors which collapse all available data and establish flow conditions for which known theoretical limits should apply.

Acknowledgements

The authors gratefully acknowledge support from NSF (grant OCI-1054966) and AFOSR (grants FA9550-12-1-0443, FA9550-17-1-0107). This work used Extreme Science and Engineering Discovery Environment (XSEDE) resources. We thank R. Bowersox, C. Pantano and J. Larsson for helpful discussions on the topics of this paper.

Appendix A

In this appendix we provide the detailed derivations and complete expressions for final forms not provided in the main section of the paper.

The leading orders of truncated integrals of m for a Gaussian distribution are given in table 3.

Similar to density (3.6), the expressions for pressure and temperature are given by:

$$p_1 = \left[\frac{\gamma - 1}{2} (M + m)^2 + 1 \right]^{-\gamma/(\gamma-1)} p_{01}, \quad (\text{A } 1a)$$

$$T_1 = \left[\frac{\gamma - 1}{2} (M + m)^2 - 1 \right]^{-1} T_{01}. \quad (\text{A } 1b)$$

Under QE, thermodynamic variables downstream of the shock will be given by RH expressions in supersonic regions:

$$p_2^> = \left[\frac{2\gamma}{\gamma - 1} (M + m)^2 - \frac{\gamma - 1}{\gamma + 1} \right] \left[\frac{\gamma - 1}{2} (M + m)^2 \right]^{-\gamma/(\gamma-1)} p_{01}, \quad (\text{A } 2a)$$

$$\begin{aligned}
 \langle m^0 \rangle^> &= \frac{1}{2} + \frac{1}{2} \operatorname{erf} \left(\sqrt{\frac{3}{2}} \frac{\Delta M}{M_t} \right) \\
 \langle m \rangle^> &= \frac{M_t}{\sqrt{6\pi}} e^{-(3/2)(\Delta M^2/M_t^2)} \\
 \langle m^2 \rangle^> &= \frac{M_t^2}{6} - \frac{\Delta M M_t}{\sqrt{6\pi}} e^{-(3/2)(\Delta M^2/M_t^2)} + \frac{M_t^2}{6} \operatorname{erf} \left(\sqrt{\frac{3}{2}} \frac{\Delta M}{M_t} \right) \\
 \langle m^0 \rangle^< &= \frac{1}{2} - \frac{1}{2} \operatorname{erf} \left(\sqrt{\frac{3}{2}} \frac{\Delta M}{M_t} \right) \\
 \langle m \rangle^< &= -\frac{M_t}{\sqrt{6\pi}} e^{-(3/2)(\Delta M^2/M_t^2)} \\
 \langle m^2 \rangle^< &= \frac{M_t^2}{6} + \frac{\Delta M M_t}{\sqrt{6\pi}} e^{-(3/2)(\Delta M^2/M_t^2)} - \frac{M_t^2}{6} \operatorname{erf} \left(\sqrt{\frac{3}{2}} \frac{\Delta M}{M_t} \right)
 \end{aligned}$$

TABLE 3. Low-order moments of m for a Gaussian distribution
 $f_m(m) = 1/M_t \sqrt{3/2\pi} e^{-(3m^2/2M_t^2)}$.

$$T_2^> = \left[\frac{2\gamma}{\gamma + 1} ((M + m)^2 - 1) + 1 \right] \left[\frac{(\gamma - 1)(M + m)^2 + 2}{(\gamma + 1)(M + m)^2} \right] \left[\frac{\gamma - 1}{2} (M + m)^2 - 1 \right]^{-1} T_{01}, \tag{A 2b}$$

while in subsonic regions we have $p_2^< \approx p_1$ and $T_2^< \approx T_1$.

These four expressions are now expanded around their respective mean as

$$q = q|_{m=0} + \left(\frac{\partial q}{\partial m} \right)_{m=0} m + \frac{1}{2} \left(\frac{\partial^2 q}{\partial m^2} \right)_{m=0} m^2 + \dots, \tag{A 3}$$

where $q = p_1, p_2^>, T_1$ or $T_2^>$.

For upstream quantities ($\langle p_1 \rangle$ and $\langle T_1 \rangle$) the averages are computed using complete integrals against the p.d.f. of m . For downstream quantities ($\langle p_2^> \rangle$ and $\langle T_2^> \rangle$) one needs to split integrals as in (3.12) to distinguish subsonic from supersonic regions:

$$\langle p_1 \rangle = \int_{-\infty}^{\infty} p_1 f_m(m) dm, \tag{A 4a}$$

$$\langle p_2^> \rangle = \int_{-\Delta M}^{\infty} p_2^> f_m(m) dm + \int_{-\infty}^{-\Delta M} p_1 f_m(m) dm, \tag{A 4b}$$

$$\langle T_1 \rangle = \int_{-\infty}^{\infty} T_1 f_m(m) dm, \tag{A 4c}$$

$$\langle T_2^> \rangle = \int_{-\Delta M}^{\infty} T_2^> f_m(m) dm + \int_{-\infty}^{-\Delta M} T_1 f_m(m) dm. \tag{A 4d}$$

Upon integration aided by the forms in table 3, the final expressions of mean pressure and temperature are

$$\langle p_1 \rangle = \mathbb{M}^{-\gamma/(\gamma-1)} p_{01} + \frac{\gamma}{12} \mathbb{M}^{(-3\gamma+2)/(\gamma-1)} [(3\gamma - 1)M^2 - 2] p_{01} M_t^2, \tag{A 5a}$$

$$\begin{aligned}
 \langle p_2 \rangle &= \left[\frac{2\gamma}{\gamma+1} M^2 - \frac{\gamma-1}{\gamma+1} \right] \mathbb{M}^{-\gamma/(\gamma-1)} p_{01} \langle m^0 \rangle^> \\
 &+ \frac{\gamma M}{\gamma+1} (-2M^2 + \gamma + 3) \mathbb{M}^{(-2\gamma+1)/(\gamma-1)} p_{01} \langle m \rangle^> \\
 &+ \frac{\gamma}{4(\gamma+1)} \mathbb{M}^{(-3\gamma+2)/(\gamma-1)} \\
 &\times [(2\gamma+2)M^4 - (3\gamma^2+8\gamma+9)M^2 + (2\gamma+6)] p_{01} \langle m^2 \rangle^> \\
 &+ \mathbb{M}^{-\gamma/(\gamma-1)} p_{01} \langle m^0 \rangle^< - \gamma M \mathbb{M}^{(-2\gamma+1)/(\gamma-1)} p_{01} \langle m \rangle^< \\
 &+ \frac{\gamma}{4} \mathbb{M}^{(-3\gamma+2)/(\gamma-1)} [(3\gamma-1)M^2 - 2] p_{01} \langle m^2 \rangle^<, \tag{A 5b}
 \end{aligned}$$

$$\langle T_1 \rangle = \mathbb{M}^{-1} T_{01} + \frac{\gamma-1}{12} \mathbb{M}^{-3} [(3\gamma-3)M^2 - 2] T_{01} M_t^2, \tag{A 5c}$$

$$\begin{aligned}
 \langle T_2 \rangle &= \left[\frac{2\gamma}{\gamma+1} (M^2 - 1) + 1 \right] \left[\frac{(\gamma-1)M^2 + 2}{(\gamma+1)M^2} \right] \mathbb{M}^{-1} T_{01} \langle m^0 \rangle^> \\
 &+ \frac{4(\gamma-1)}{(\gamma+1)^2 M^3} T_{01} \langle m \rangle^> - \frac{6(\gamma-1)}{(\gamma+1)^2 M^4} T_{01} \langle m^2 \rangle^> \\
 &+ \mathbb{M}^{-1} T_{01} \langle m^0 \rangle^< - (\gamma-1) M \mathbb{M}^{-2} T_{01} \langle m \rangle^< \\
 &+ \frac{\gamma-1}{4} \mathbb{M}^{-3} [3(\gamma-1)M^2 - 2] T_{01} \langle m^2 \rangle^<, \tag{A 5d}
 \end{aligned}$$

where, as in the main text, we have defined $\mathbb{M} = (\gamma - 1)M^2/2 + 1$ for convenience. The ratio of the corresponding expressions yield the expressions denoted in (3.15) and (3.16).

A similar procedure is followed to obtain the entropy jump (3.19). In terms of supersonic and subsonic regions we write

$$\langle \Delta s \rangle = C_p (\langle \ln T_2 \rangle^> - \langle \ln T_1 \rangle^>) - R (\langle \ln p_2 \rangle^> - \langle \ln p_1 \rangle^>) + \alpha_s C_p (\gamma - 1)^2 M_t^4 \langle m^0 \rangle^<, \tag{A 6}$$

which requires the evaluation of $\langle \ln T_1 \rangle$ (as in (3.21)), $\langle \ln T_2 \rangle$, $\langle \ln p_1 \rangle$ and $\langle \ln p_2 \rangle$. Again using QE, the logarithm of pressure and temperature can be expanded in Taylor series and integrated in the appropriate probability space to obtain

$$\begin{aligned}
 \langle \ln p_1 \rangle^> &= \ln(\mathbb{M}^{-\gamma/(\gamma-1)} \langle m^0 \rangle^>) - \frac{2\gamma M}{(\gamma-1)M^2 + 2} \langle m \rangle^> \\
 &+ \frac{\gamma}{4} [(\gamma-1)M^2 - 2] \mathbb{M}^{-2} \langle m^2 \rangle^> + \ln p_{01} \langle m^0 \rangle^>, \tag{A 7a}
 \end{aligned}$$

$$\begin{aligned}
 \langle \ln p_2 \rangle^> &= \ln \left(\left[\frac{2\gamma}{\gamma+1} M^2 - \frac{\gamma-1}{\gamma+1} \right] \mathbb{M}^{-\gamma/(\gamma-1)} \right) \langle m^0 \rangle^> \\
 &+ \frac{\gamma M (-2M^2 + \gamma + 3)}{2\gamma M^2 - \gamma + 1} \mathbb{M}^{-1} \langle m \rangle^> \\
 &+ \gamma \left[-\mathbb{M}^{-2} + \frac{\mathbb{M}^{-1}}{2} + \frac{4-4\gamma}{(-2\gamma M^2 + \gamma - 1)^2} - \frac{2}{(2\gamma M^2 - \gamma + 1)} \right] \langle m^2 \rangle^> \\
 &+ \ln p_{01} \langle m^0 \rangle^>, \tag{A 7b}
 \end{aligned}$$

$$\begin{aligned}
\langle \ln T_2 \rangle &= \ln \left(\left[\frac{2\gamma}{\gamma+1}(M^2-1) + 1 \right] \left[\frac{(\gamma-1)M^2+2}{(\gamma+1)M^2} \mathbb{M}^{-1} \right] \langle m^0 \rangle^> \right. \\
&\quad + \frac{2(\gamma-1)}{2\gamma M^3 - \gamma M + M} \langle m \rangle^> - \frac{(\gamma-1)[\gamma(6M^2-1)+1]}{(2\gamma M^3 - \gamma M + M)^2} \langle m^2 \rangle^> \\
&\quad \left. + \ln T_{01} \langle m^0 \rangle^> \right. \quad (A\ 7c)
\end{aligned}$$

These expressions can be combined into (A 6) to obtain $g_s(M, M_t)$ in (3.23).

REFERENCES

- AGUI, J. H., BRIASSULIS, G. & ANDREOPOULOS, Y. 2005 Studies of interactions of a propagating shock wave with decaying grid turbulence: velocity and vorticity fields. *J. Fluid Mech.* **524**, 143–195.
- ANDREOPOULOS, Y., AGUI, J. H. & BRIASSULIS, G. 2000 Shock wave–turbulence interactions. *Annu. Rev. Fluid Mech.* **32**, 309–345.
- BARENBLATT, G. I. 2003 *Scaling*. Cambridge University Press.
- BARRE, S., ALEM, D. & BONNET, J. P. 1996 Experimental study of a normal shock/homogeneous turbulence interaction. *AIAA J.* **34**, 968–974.
- BATCHELOR, G. K. 1953 *The Theory of Homogeneous Turbulence*. Cambridge University Press.
- BOUKHARFANE, R., BOUALI, Z. & MURA, A. 2018 Evolution of scalar and velocity dynamics in planar shock–turbulence interaction. *Shock Waves* **28** (6), 1117–1141.
- CHISNELL, R. F. 1955 The normal motion of a shock wave through a non-uniform one-dimensional medium. *Proc. R. Soc. Lond. A* **232** (1190), 350–370.
- DONZIS, D. A. 2012a Amplification factors in shock–turbulence interactions: effect of shock thickness. *Phys. Fluids* **24**, 011705.
- DONZIS, D. A. 2012b Shock structure in shock–turbulence interactions. *Phys. Fluids* **24**, 126101.
- DONZIS, D. A. & JAGANNATHAN, S. 2013 Fluctuations of thermodynamic variables in stationary compressible turbulence. *J. Fluid Mech.* **733**, 221–244.
- FREUND, J. B. 1997 Proposed inflow/outflow boundary condition for direct computation of aerodynamic sound the vorticity jump across a shock in a non-uniform flow. *AIAA J.* **35** (4), 740–742.
- GATSKI, T. B. & BONNET, J.-P. 2009 *Compressibility, Turbulence and High Speed Flow*. Elsevier.
- GOLDENFELD, N. 2006 Roughness-induced critical phenomena in a turbulent flow. *Phys. Rev. Lett.* **96**, 044503.
- GRANT, H. L. & NISBET, I. C. T. 1957 The inhomogeneity of grid turbulence. *J. Fluid Mech.* **2** (3), 263–272.
- HANNAPPEL, R. & FRIEDRICH, R. 1995 Direct numerical-simulation of a Mach-2 shock interacting with isotropic turbulence. *Appl. Sci. Res.* **54**, 205–221.
- HESSELINK, L. & STURTEVANT, B. 1988 Propagation of weak shocks through a random medium. *J. Fluid Mech.* **196**, 513–553.
- HONKAN, A. & ANDREOPOULOS, J. 1992 Rapid compression of grid-generated turbulence by a moving shock-wave. *Phys. Fluids* **4** (11), 2562–2572.
- INOKUMA, K., WATANABE, T., NAGATA, K., SASOH, A. & SAKAI, Y. 2017 Finite response time of shock wave modulation by turbulence. *Phys. Fluids* **29** (5), 051701.
- JACQUIN, L., CAMBON, C. & BLIN, E. 1993 Turbulence amplification by a shock wave and rapid distortion theory. *Phys. Fluids* **3**, 2539.
- JAGANNATHAN, S. & DONZIS, D. A. 2016 Reynolds and Mach number scaling in solenoidally-forced compressible turbulence using high-resolution direct numerical simulations. *J. Fluid Mech.* **789**, 669–707.

- JAMME, S., CAZALBOU, J.-B., TORRES, F. & CHASSAING, P. 2002 Direct numerical simulation of the interaction between a shock wave and various types of isotropic turbulence. *Flow Turbul. Combust.* **68**, 227–268.
- JIMENEZ, J. 1998 Turbulent velocity fluctuations need not be Gaussian. *J. Fluid Mech.* **376**, 139–147.
- KITAMURA, T., NAGATA, K., SAKAI, Y. & ITO, Y. 2016 Rapid distortion theory analysis on the interaction between homogeneous turbulence and a planar shock wave. *J. Fluid Mech.* **802**, 108–146.
- KOVASZNY, L. S. G. 1953 Turbulence in supersonic flow. *J. Aerosp. Sci.* **20** (10), 657–674.
- LARSSON, J., BERMEJO-MORENO, I. & LELE, S. K. 2013 Reynolds- and Mach-number effects in canonical shock–turbulence interaction. *J. Fluid Mech.* **717**, 293–321.
- LARSSON, J. & LELE, S. K. 2009 Direct numerical simulation of canonical shock/turbulence interaction. *Phys. Fluids* **21**, 126101.
- LEE, S., LELE, S. K. & MOIN, P. 1993 Direct numerical simulation of isotropic turbulence interacting with a weak shock wave. *J. Fluid Mech.* **251**, 533–562.
- LEE, S., LELE, S. K. & MOIN, P. 1997 Interaction of isotropic turbulence with shock waves: effect of shock strength. *J. Fluid Mech.* **340**, 225–247.
- LELE, S. K. 1992a Compact finite-difference schemes with spectral-like resolution. *J. Comput. Phys.* **103**, 16–42.
- LELE, S. K. 1992b Shock-jump relations in a turbulent flow. *Phys. Fluids* **4** (12), 2900–2905.
- LIVESCU, D. & RYU, J. 2016 Vorticity dynamics after the shock–turbulence interaction. *Shock Waves* **26** (3), 241–251.
- MAHESH, K., LEE, S., LELE, S. K. & MOIN, P. 1995 Interaction of an isotropic field of acoustic waves with a shock wave. *J. Fluid Mech.* **300**, 383–407.
- MAHESH, K., LELE, S. K. & MOIN, P. 1997 The influence of entropy fluctuations on the interaction of turbulence with a shock wave. *J. Fluid Mech.* **334**, 353–379.
- MOECKEL, W. E. 1952 Interaction of oblique shock waves with regions of variable pressure, entropy, and energy. *NACA TN-2725*.
- MOHAMED, M. S. & LARUE, J. C. 1990 The decay power law in grid-generated turbulence. *J. Fluid Mech.* **219**, 195–214.
- MOIN, P. & MAHESH, K. 1998 Direct numerical simulation: A tool in turbulence research. *Annu. Rev. Fluid Mech.* **30**, 539–578.
- MONIN, A. S. & YAGLOM, A. M. 1975 *Statistical Fluid Mechanics*, vol. II. MIT Press.
- MOORE, F. K. 1954 Unsteady oblique interaction of a shock wave with a plane disturbance. *Tech. Rep. NACA Rep.* 1165.
- MOSER, R. D. 2006 On the validity of the continuum approximation in high Reynolds number turbulence. *Phys. Fluids* **18** (7), 078105.
- NOULLEZ, A., FRISCH, U., WALLACE, G., LEMPET, W. & MILES, R. B. 1997 Transverse velocity increments in turbulent flow using the relief technique. *J. Fluid Mech.* **339**, 287–307.
- OBUKHOV, A. M. 1949 The structure of the temperature field in a turbulent flow. *Izv. Akad. Nauk. SSSR* **13**, 58–69.
- QUADROS, R., SINHA, K. & LARSSON, J. 2016a Kovasznay mode decomposition of velocity–temperature correlation in canonical shock–turbulence interaction. *Flow Turbul. Combust.* **97**, 787–810.
- QUADROS, R., SINHA, K. & LARSSON, J. 2016b Turbulence energy flux generated by shock/homogeneous–turbulence interaction. *J. Fluid Mech.* **796**, 113–157.
- RIBNER, H. S. 1954a Convection of a pattern of vorticity through a shock wave. *NACA TR-1164*.
- RIBNER, H. S. 1954b Shock–turbulence interaction and the generation of noise. *NACA TR-1233*.
- RYU, J. & LIVESCU, D. 2014 Turbulence structure behind the shock in canonical shock–vortical turbulence interaction. *J. Fluid Mech.* **756**, R1.
- SAGAUT, P. & CAMBON, C. 2008 *Homogeneous Turbulence Dynamics*. Cambridge University Press.
- SCHUMACHER, J., SCHEEL, J. D., KRASNOV, D., DONZIS, D. A., YAKHOT, V. & SREENIVASAN, K. R. 2014 Small-scale universality in fluid turbulence. *Proc. Natl Acad. Sci. USA* **111** (30), 10961–10965.

- SCHUMACHER, J., SREENIVASAN, K. R. & YAKHOT, V. 2007 Asymptotic exponents from low-Reynolds-number flows. *New J. Phys.* **9**, 89.
- TANAKA, K., WATANABE, T., NAGATA, K., SASOH, A., SAKAI, Y. & HAYASE, T. 2018 Amplification and attenuation of shock wave strength caused by homogeneous isotropic turbulence. *Phys. Fluids* **30** (3), 035105.
- TAYLOR, G. I. 1935 Turbulence in a contracting stream. *Z. Angew. Math. Mech.* **15**, 91–96.
- THOMPSON, P. A. 1984 *Compressible Fluid Dynamics*. McGraw-Hill.
- VELIKOVICH, A. L., HUETE, C. & WOUCHUK, J. G. 2012 Effect of shock-generated turbulence on the Hugoniot jump conditions. *Phys. Rev. E* **85**, 016301.
- WHITHAM, G. B. 1958 On the propagation of shock waves through regions of non-uniform area or flow. *J. Fluid Mech.* **4** (4), 337–360.
- WIDOM, B. 1965 Equation of state in the neighborhood of the critical point. *J. Chem. Phys.* **43** (11), 3898–3905.
- WILLIAMS, J. E. F. & HOWE, M. S. 1973 On the possibility of turbulent thickening of weak shock waves. *J. Fluid Mech.* **58** (3), 461–480.
- WOUCHUK, J. G., DE LIRA, C. H. R. & VELIKOVICH, A. L. 2009 Analytical linear theory for the interaction of a planar shock wave with an isotropic turbulent vorticity field. *Phys. Rev. E* **79**, 066315.
- YAKHOT, V. & DONZIS, D. A. 2017 Emergence of multiscaling in a random-force stirred fluid. *Phys. Rev. Lett.* **119**, 044501.
- YAKHOT, V. & DONZIS, D. A. 2018 Anomalous exponents in strong turbulence. *Phys. D* **384–385**, 12–17.
- ZANK, G. P., ZHOU, Y., MATTHAEUS, W. H. & RICE, W. K. M. 2002 The interaction of turbulence with shock waves: a basic model. *Phys. Fluids* **14**, 3766–3774.
- ZELDOVICH, Y. B. & RAIZER, Y. P. 2002 *Physics of Shock Waves and High-Temperature Hydrodynamic Phenomena*. Dover.